Sentinel-1 Detection of Ice Slabs on the Greenland Ice Sheet

Riley Culberg[1], Roger J. Michaelides[2], and Julie Z. Miller[3]

[1]Department of Earth and Atmospheric Sciences, Cornell University
[2]Department of Earth, Environmental, and Planetary Sciences, Washington University in St. Louis
[3]Earth Science and Observation Center, Cooperative Institute for Research in Environmental Sciences, University of Colorado Boulder

Correspondence: Riley Culberg (rtculberg@cornell.edu)

Abstract. Ice slabs are multi-meter thick layers of refrozen ice that limit meltwater storage in firn, leading to enhanced surface runoff and ice sheet mass loss. To date, ice slabs have primarily been mapped using airborne ice-penetrating radar, which has limited spatial and temporal coverage. This makes it difficult to fully assess the current extent and continuity of ice slabs or to validate predictive models of ice slab evolution that are key to understanding their impact on Greenland's surface mass balance. Here, for the first time, we map the extent of ice slabs and superimposed ice facies across the entire Greenland Ice Sheet at 500 m resolution using dual-polarization Sentinel-1 (S-1) synthetic aperture radar data collected in winter 2016-2017. ~~for The~~ We do this by selecting empirical thresholds for the cross-polarized backscatter ratio (HV - HH) and HV backscattered power that jointly optimize agreement between airborne ice-penetrating radar data detections of ice slabs and the S-1 ~~inferred~~ estimates of ice slab extent~~is in excellent agreement with ice-penetrating radar ice slab detections from spring 2017, as well as the extent of the visible runoff zone as mapped from optical imagery. Our results show~~ . Our results show that there is a strong correlation between C-band backscatter and the ice content of the upper $\sim$ 7 meters of the firn column that enables ice slab mapping with S-1. Our new mapping shows that ice slabs are nearly continuous around the entire margin of the ice sheet~~, including~~ . This includes regions in Southwest Greenland where ice slabs have not been previously identified, but where the S-1 inferred ice slab extent shows strong agreement with the extent of visible runoff mapped from optical imagery. The algorithm developed here ~~also~~ lays the groundwork for long-term monitoring of ice slab expansion with current and future C-band satellite systems and highlights the potential added value of future L-band missions for near-surface studies in Greenland.

1 Introduction

Over the last two decades, ~~more than~~ around half of mass loss from the Greenland Ice Sheet (GrIS) has come from the runoff of surface meltwater (Van Den Broeke et al., 2009; Enderlin et al., 2014; Mouginot et al., 2019) , with the remaining 45-50% attributable to ice dynamical processes and ice-ocean interactions in marine terminating sectors . However, surface processes are projected to remain the dominant contributor to Greenland's sea level contribution over the next century, particularly as the ice margin retreats onto land above sea level (Fox-Kemper et al., 2021). By extension, much of the uncertainty in future mass loss from the ice sheet can also be ascribed to uncertainty in surface processes (Fox-Kemper et al., 2021). One such process that remains poorly constrained is the development and expansion of ice slabs in firn, particularly near the equilibrium line. Ice slabs are multi-meter thick layers of refrozen ice that form just below the surface (Machguth et al., 2016) and can be horizontally continuous over tens of kilometers (MacFerrin et al., 2019). As a result, ice slabs are largely impermeable and limit the vertical percolation of meltwater into the underlying relict firn, leading to a rapid transition from meltwater retention to runoff as they form (Machguth et al., 2016; MacFerrin et al., 2019; Tedstone and Machguth, 2022). To date, ice slabs have primarily been mapped using Operation IceBridge (OIB) airborne ice-penetrating radar surveys, as these data directly resolve the vertical structure of the subsurface and can distinguish homogeneous refrozen ice bodies from lower density firn (MacFerrin et al., 2019; Jullien et al., 2023). These data have shown that ice slabs dominate the wet snow zone along the western, northern, and northeastern coasts of Greenland. The southeast basin is the only major region where ~~no~~ limited ice slabs have been detected, due to the high snow accumulation rate that insulates subsurface liquid water from refreezing and ~~preferences~~ leads to the formation of perennial firn aquifers instead (Forster et al., 2014; Munneke et al., 2014).

While the OIB data have provided critical insights into ice slab extent across the GrIS, these data are significantly limited in both space and time. Data are only available directly beneath the aircraft flight track, and collection was limited to a moderate number of flight lines in spring (typically April or May) each year from 2011-2014 and 2017-2018, along with a few additional flights over the wet snow zone in 2010. These gaps in coverage lead to a number of issues. In many regions, the upper elevation limit of the ice slabs is poorly defined, due to a lack of flights perpendicular to the coastline, and there are some areas, most notably in southern Greenland and on peripheral ice caps, where there is insufficient flight coverage to assess whether ice slabs are even present. Even in regions of good coverage, there are typically 5-20 km gaps between flight lines. As a result, the full extent of ice slabs on the GrIS remains poorly defined and it has been difficult to fully assess the km-scale continuity of this facie. Additionally, there are very few repeated flights that were flown perpendicular to the coastline, which are required to robustly assess the inland expansion of ice slabs from year to year. Jullien et al. (2023) showed that some ice slab growth occurred between the period from 2010-2012 to 2017-2018, but the ~~spatial resolution~~ resolution and coverage of that analysis ~~was coarse and limited by~~ limited by large spatial data gaps and the need to aggregate multiple years of data to achieve reasonable coverage of the whole ice sheet. With the end of the OIB mission in 2019, there ~~is no new~~ are no current or planned ice-penetrating radar ~~data~~ missions to improve these time series or to assess the impact of more recent heavy melt seasons, ~~which included the first high elevation rain event,~~ such as 2019, 2021, and 2023~~(Tedesco and Fettweis, 2020; Harper et al., 2023; Box et al., 2023)~~, which included a significant high elevation rain event in August 2021 (Tedesco and Fettweis, 2020; Box et al., 2022, 2023).

These spatial and temporal gaps significantly impede our ability to assess the impact of ice slab development and expansion on the current and future mass balance of the GrIS. For example, MacFerrin et al. (2019) parameterized ice slab extent as a function of the ten-year running mean of local excess melt and applied this parameterization to an ensemble of regional climate models to predict that ice slab expansion would add 7-74 mm of additional sea level rise by 2100. However, this excess melt threshold was tuned by matching the modeled ice slab extent to the aggregate observed extent from 2010-2014 (MacFerrin et al., 2019). As a result, it remains unclear whether the temporal evolution of ice slabs in this model accurately captures the true pace of ice slab growth. ~~As firn models continue to improve, there are many opportunities to implement~~ Recently, more physics-based ~~estimates of ice slab expansion and runoff contributions~~models of firn hydrology have been used to model climatic drivers of ice slab extent and expansion (Brils et al., 2024), but in the absence of validating data, significant uncertainties in future projections will remain.

The only clear mechanism for mapping ice slab extent across the entire ice sheet at high resolution (∼1 km or better) on an annual or better basis is to use satellite microwave remote sensing systems. In fact, ice slabs have been mapped from space using the L-band radiometer onboard the Soil Moisture Active Passive (SMAP) mission ~~by Miller et al. (2022a)~~in Miller et al. (2022a, b). However, there are ~~significant limitations to this approach~~limitations to that algorithm. In particular, the instrument resolution is approximately 30 km (Miller et al., 2022a), making it difficult to clearly define the inland extent of the ice slabs ~~or~~ and impossible to capture expansion on the order of a few kilometers or less per a year. Additionally, although rough estimates of the interannual variability are given, this algorithm aggregates ∼5 years of ~~radar~~ radiometer data to create a single estimate of ice slab extent to create higher probability maps (Miller et al., 2022a), which limits its use for generating long time series. There are also notable discrepancies between the SMAP and OIB ice slab extents, particularly in the Northwest where SMAP fails to detect large swaths of the OIB-detected ice slabs, and in the North and Northeast where SMAP places the ice slabs at higher elevations than the OIB data (see Figure 11).

An alternate approach is to use active synthetic aperture radar systems such as the ~~European Space Agency's (ESA)~~ ESA Sentinel-1 (S-1) series satellites (Berger et al., 2012). Since C-band radio waves penetrate roughly 5-15 meters into snow, firn, and ice, depending on the local physical and ~~dieletric~~ dielectric properties (Rignot et al., 2001; Hoen, 2001; Fischer et al., 2019), the depth-integrated surface echo measured by the instrument mainly contains information about the near-surface structure. In Extra Wide Swath mode, Sentinel-1 covers the entire GrIS approximately every 10 days with a spatial resolution of 20 x 40 meters and ~~a full catalog of data~~ data are available from late 2014 to the present day. With the anticipated launches of Sentinel-1C & D, the data record is projected to continue uninterrupted through at least the early 2030s. Therefore, Sentinel-1 could not only provide the first pan-Greenland mapping of ice slabs at high-resolution, but such an algorithm would open the door to long-term monitoring of ice slab expansion, potentially covering close to two decades of observations. Here, we develop an algorithm to map refrozen ice facies on the Greenland Ice Sheet using dual polarization Extra Wide ~~swath~~ Swath Sentinel-1 measurements of radar backscatter in conjunction with calibration data from ice-penetrating radar observations.

2 Electromagnetic Interactions in Firn

On ice sheets, mean firn density increases exponentially with depth as it compacts under its own weight (Bader, 1954; Herron and Langway, 1980). In the percolation zone, the structure is further modified by the infiltration and refreezing of surface meltwater that forms ice lenses and ice pipes (Benson, 1962). Ice lenses are horizontal sheets of refrozen solid ice that may be up to a few tens of ~~cms~~ centimeters thick and extend laterally for a few meters (Benson, 1962; MacFerrin et al., 2019), while ice pipes are vertical refrozen conduits that represent preferential infiltration pathways connecting these ice lenses (Marsh and Woo, 1984; Pfeffer and Humphrey, 1998; Humphrey et al., 2012). The proportion of the firn column occupied by these refreeze features generally increases with decreasing elevation and increasing melt-to-accumulation ratio (Harper et al., 2012; Machguth et al., 2016). In the extreme, consistent excess melting may anneal these ice lenses together into multi-meter thick ice

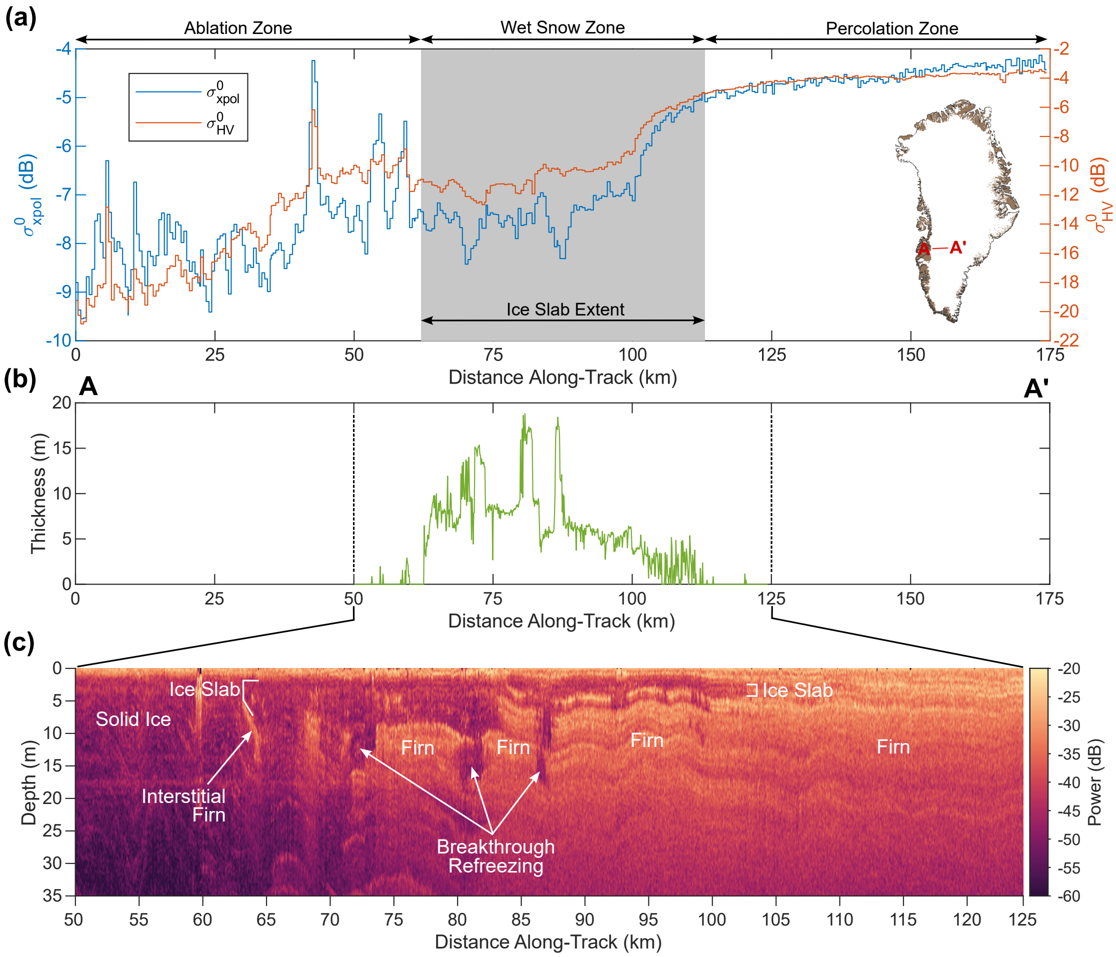

Figure 1. Radar signatures of ice slabs along a transect in Southwest Greenland. ~~(Contains modified Copernicus Sentinel data 2016-2017, processed by ESA.)~~ a) Sentinel-1 σ^0_{HV} is shown in red and the cross-pol backscatter ratio, $\sigma^0_{xpol} = \sigma^0_{HV} - \sigma^0_{HH}$ is shown in blue. The gray region denotes where ice slabs have been detected with ice-penetrating radar (Culberg et al., 2022b). b) Ice slab thickness along the transect as measured with ice-penetrating radar (Culberg et al., 2022b). There is a rapid, down-flow decrease in σ^0_{xpol} as the ice slab thickens, with the backscatter ~~saturating~~ plateauing once the ice slab reaches a thickness of around 7 m. The inset map (Gerrish, 2020; Morlighem et al., 2017) shows the location of this transect in Southwest Greenland. c) Radargram from April 2015 collected by the Ultrawideband MCoRDS system (Paden et al., 2014a) showing the subsurface structure in the region where ice slabs have been detected. In the percolation zone, the structure is dominated by layered firn with strong scattering from ~~small~~ embedded ice features. In the wet snow zone, a thick layer of homogeneous refrozen ice with low backscatter overlies relict firn. In the ablation zone, only solid ice remains and there is relatively low backscatter at all depths due to the absence of density ~~constrasts~~ contrasts in the subsurface. (Note: This figure contains modified Copernicus Sentinel data 2016-2017, processed by ESA.)

slabs that form in the wet snow zone (MacFerrin et al., 2019; Machguth et al., 2016). The wet snow facies eventually transition to the ablation zone via a region of superimposed ice facies, where the near-surface ice is formed by refreezing within the annual accumulation (Benson, 1962). At the lowest elevations, where annual melting consistently exceeds accumulation, the ice sheet transitions to the bare ice ablation zone composed of homogeneous meteoric ice that is exposed at the surface via horizontal advection and ablation.

These near-surface structural variations with elevation lead to commensurate changes in the dominant electromagnetic scattering mechanisms. In the percolation zone, radar echoes are thought to be dominated by volume scattering from embedded ice features on the scale of a few wavelengths (Fahnestock et al., 1993; Jezek et al., 1994; Rignot, 1995; Baumgartner et al., 1999; Langley et al., 2009), making the GrIS percolation zone one of the most radio bright regions on Earth (Swift et al., 1985; Rignot et al., 1993; Jezek et al., 1994). Past work has ~~successfully~~ modeled the observed percolation zone backscatter at C-band as volume scattering from randomly oriented cylinders (Rignot, 1995). This volume scattering dominated regime also leads to significant depolarization of the incident wave and a large radar cross-section in the cross-polarized (HV or VH) channels (Jezek et al., 1993; Rignot, 1995; Langley et al., 2007; Barzycka et al., 2019). By contrast, scattering in the bare ice ablation zone is dominated by rough surface scattering at the air-ice interface, with relatively little volume scattering since heterogeneities such as air bubbles are significantly smaller than the C-band wavelength (Langley et al., 2007, 2009; Barzycka et al., 2019). As a result, the radar cross section of the ablation zone is relatively ~~small~~ low and little depolarization occurs, so the echoes are dominated by co-polarized (HH or VV) returns (Langley et al., 2007, 2009). Numerous papers have mapped glacier facies on Arctic ice caps and mountain glaciers based on these characteristic changes in backscatter (Partington, 1998; Long and Drinkwater, 1994; Barzycka et al., 2019). For example, Langley et al. (2008) demonstrated that on Kongsvegen Glacier in Svalbard, the boundaries between firn, superimposed ice, and glacier ice could be mapped in C-Band ENVISAT SAR data from the ∼5 dB change in backscatter between each region, with ground-penetrating radar used to validate the mapping.

Ice slab regions likely represent an intermediate scattering regime between the percolation zone and superimposed ice or ablation zones, with ~~a balance of~~ both surface and volume scattering contributing to the total backscatter. Nadir-looking airborne radar sounding measurements show that ice slabs are characterized by strong reflections from their upper and lower interfaces, but very low backscatter within the refrozen ice itself (MacFerrin et al., 2019; Jullien et al., 2023). However, the presence of remnant interstitial firn layers does lead to overall higher radar sounder backscatter in these refrozen ice facies than in meteoric ice (Figure 1c). Side-looking synthetic aperture radar returns from ice slabs display lower σ^0_{xpol} than the percolation zone, but higher values than the upper ablation zone, which could be interpreted as greater surface scattering and lower volume scattering than the percolation zone, but higher volume scattering than meteoric ice in the lower ablation zone. ~~Figure 1a-b~~

Figure 1a-b shows an example of this effect along a transect from the ice margin ~~to~~ up to the shallow percolation zone in Southwest Greenland. The percolation zone HV backscatter (σ^0_{HV}) is consistently about ~~-2~~ -4 dB, but decays at lower elevations as ice slabs begin to form and thicken, eventually ~~reaching a new plateau around~~ plateauing around an average of -11 dB ~~.~~ across the upper ablation and wet snow zones. However, there is significant local variability in these regions, with the HV backscatter varying from -13 dB to -6 dB around the mean. The ratio of the HV to HH backscatter ($\sigma^0_{xpol} = \sigma^0_{HV} - \sigma^0_{HH}$ (in dB)), known at the cross-polarized backscatter ratio (Ulaby and Long, 2014) or linear backscatter ratio (Rignot, 1995), has been used as a proxy for the ratio of volume to surface scattering in the Greenland percolation zone (Rignot, 1995) and is also responsive to this change in subsurface structure, decreasing from -4.5 dB to -7.5 dB as ice slabs develop at the test site. In this paper, we exploit this reduction in volume scattering that occurs as ice slabs form to map ice slabs from S-1 C-band winter backscatter measurements.

3 Methods

3.1 Sentinel-1 Backscatter Mosaics

For this analysis, we use Extra Wide Swath (EW) ground range detected (GRD) Sentinel-1A & B data collected in HH and HV polarizations at a center frequency of 5.405 GHz (ESA, 2023) over the GrIS from ~~1~~ 01 October 2016 to 30 April 2017. We focus on a single year of measurements to demonstrate the feasibility of mapping ice slabs with S-1 without confounding complications from instrument radiometric stability, evolving observation strategies, and multi-annual changes in surface scattering properties. Only ∼10 days of data are needed to fully cover the entire ice sheet, but we choose to use the full winter period because the extra observations allow us to develop a robust mean backscatter map that reduces the influence of temporal variability in scattering properties, speckle, and variable incidence angles. We expect ice slab extent to be stable during this period since there is no melt infiltration. We only use winter data because the presence of surface meltwater ~~enhances~~ increases both the surface dielectric contrast and the near-surface attenuation in water-saturated layers, obscuring the subsurface structure. Due to the huge data volume, we process these data in Google Earth Engine (GEE) (Gorelick et al., 2017). Data in the GEE S-1 GRD data collection have undergone thermal noise removal, radiometric calibration, geometric terrain correction, and conversion to dB values in the Sentinel-1 Toolbox before being posted to the cloud. Unfortunately, these data have not undergone radiometric terrain correction, and it is impossible to fully implement this algorithm in GEE since it requires access to the data in the original radar coordinates. We experimented with applying an angle-based radiometric terrain correction method designed for GEE (Vollrath et al., 2020), but found that it produced little to no change in the backscatter values due to the extremely low surface slopes on most of the ice sheet. Therefore, we do not implement this correction in our final workflow.

With both Sentinel-1A and Sentinel-1B in operation, the exact repeat interval for any point on the ice sheet is 6 days. However, because the EW swath width is 410 km and Greenland is at high latitudes, the coverage is often more frequent. During our 7 month study period, the average number of observations per pixel was 190, or almost one observation per day, with a minimum of 29 and a maximum of 571 observations. ~~The number of observations is highest in the north and around the margins and lowest in the interior southern saddle.~~ Within each observing pass, the incidence angle varies from 18.9° to 47° across ~~swath (ESA, 2023), which creates a significant challenge for generating a consistent backscatter mosaic for the entire ice sheet~~the swath (ESA, 2023). Particularly in the percolation zone, backscatter varies strongly with incidence angle, which leads to obvious seams between overlapping swaths and spatial variations in backscatter that are attributable to observation geometry rather than physical properties of the ice sheet. ~~Studies using~~ Additionally, the data are subject to speckle and temporal variations in backscatter due to snowfall, wind scour, and other environmental factors that impact the surface scattering structure. All of these factors lead to significant challenges in generating a single consistent backscatter mosaic for the entire ice sheet.

To reduce speckle, we first multilook all images to 500 m resolution, which effectively balances speckle suppression and data resolution (see the Supplementary Information for a resolution sensitivity analysis). Following prior studies with C- and L-band satellite radar scatterometery data ~~often exploit~~ over ice sheets, we then infer a linear relationship between incidence angle and backscatter to correct for ~~these~~ incidence angle variations ~~across the swath (Long and Drinkwater, 1994; Ashcraft and Long, 2005; Lindsley . However, the coefficients of this linear fit vary with region and time(Lindsley and Long, 2016; Long and Miller, 2023). Thereforeto correct for the effects on incidence angle in our mosaic~~in space and time(Long and Drinkwater, 1994; Ashcraft and Long, 2005; Lindsley a . Therefore, we fit a linear function to incidence angle vs backscatter on a per-pixel basis using all available images in our study period~~and then use this relationship~~ . We then use these relations to calculate the theoretical backscatter at an incidence angle of 35° ~~. Scatterometer~~ in each pixel. Radar scatterometry studies have typically corrected their data to an incidence angle of 40°, but ~~here we choose a~~ we choose to correct the data to an incidence angle close to the middle of the S-1 scene. We combine both ascending and descending orbits from both satellites to maximize the angular diversity in each pixel for the most robust fit and ~~apply a separate empirical linear to correction to~~ calculate a separate linear fit the σ^0_{HH} and σ^0_{HV} measurements.

The Supplementary Information provides detailed information on the backscatter residuals after correction and the sensitivity of the final results to the angular diversity and number observations per pixel. Overall, we find that the residuals are generally less than ± 1 dB and most large residuals are driven by non-stationary backscatter time series in regions with subsurface meltwater,like firn aquifers or subsurface lakes, rather than a failure of the linear fit. However, we also observe large residuals in peripheral regions of the ice sheet and on small ice caps with steep terrain. The final ice slab classification results are insensitive to angular diversity or number of observations as long as there are a median of at least ~117 observations per pixel spanning at least 10 unique incidence angles, a criterion which is met for our study area.

Our linear fit method not only removes backscatter variations due to observing geometry, but also serves to average all available observations in each pixel. This further reduces speckle and averages out temporal variations in backscatter over the winter season. In this way, we form ~~a~~ consistent mean winter ~~backscatter image~~ backscatters mosaics for the entire ice sheet for each polarization. We then calculate the σ^0_{xpol} map by subtracting the σ^0_{HH} map from the σ^0_{HV} map. ~~Before further analysis, we multi-look each mosaic to 500m square pixels with a boxcar filter and export the data as unsigned 16 bit integers. We also~~ Finally, we use the BedMachinev3 ice mask to remove pixels in regions without ice (Morlighem et al., 2017).

Figure 2a-b shows the mean winter σ^0_{HV} and σ^0_{xpol} mosaics for Greenland in winter 2016-2017. Regions with ice slabs clearly show greater σ^0_{HV} than the lower ablation zone, but reduced σ^0_{HV} compared with the percolation zone. Similarly, ice slabs show a lower σ^0_{xpol} than the percolation zone.

3.2 Excluding the Dry Snow Zone and Firn Aquifer Regions

In order to reduce false positive detection of ice slabs, we exclude regions of the ice sheet that a) experience little to no melting or b) are already known to host firn aquifers from further analysis. This step is critical because, as can be seen in Figure~~2b~~ 2b, both of these regions exhibit low σ^0_{xpol} values that are on par with what is observed in known ice slab regions. In the dry snow

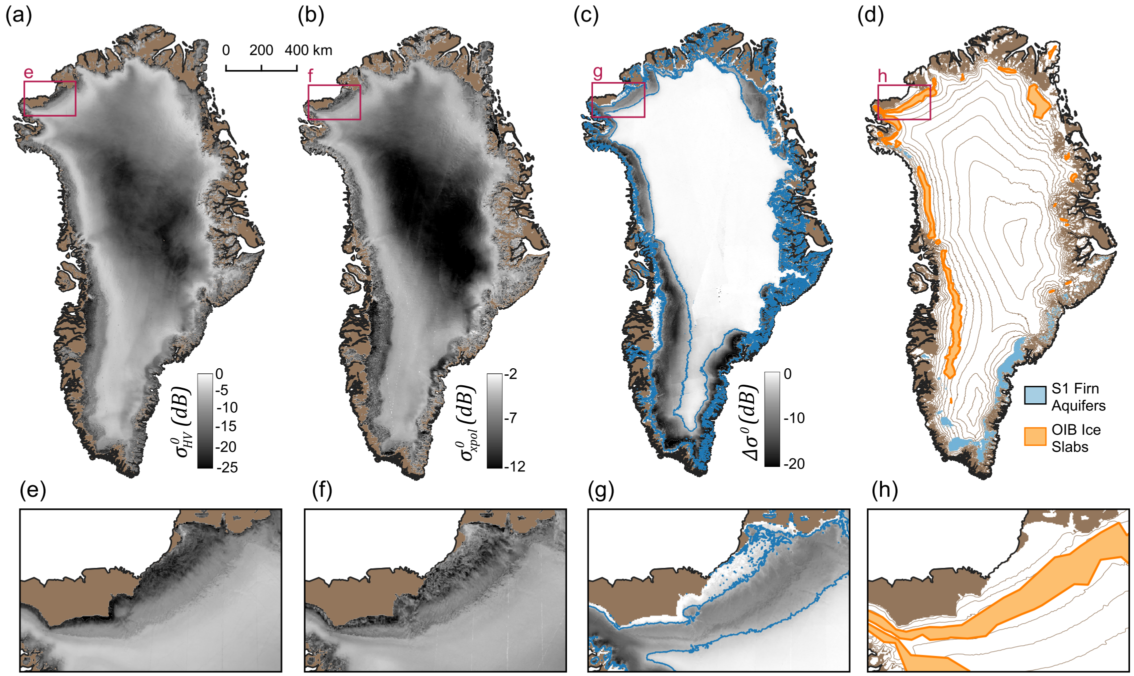

Figure 2. a) Average winter σ^0_{HV} map at 35^o incidence angle covering 1 Oct 2016 - 30 April 2017. b) Average winter σ^0_{xpol} map at 35^o incidence angle covering 1 Oct 2016 - 30 April 2017. c) Difference between summer and winter HH backscatter ($\Delta\sigma^0$), averaged over 1 Nov 2014 - 31 Aug 2020 . We ~~exclude all~~ only consider the regions ~~outside~~ inside the blue ~~overlay from~~ outline for our ice slab analysis, since the ~~minimal~~ large change in backscatter between seasons (dark color) indicates that there is ~~relatively little~~ significant annual surface ~~melting~~ melt retained in surface snow in these areas. d) Locations of firn aquifers (blue) detected using Sentinel-1 data from 2014-2019 as published in Brangers et al. (2020). Regions detected as ice slabs with ice-penetrating radar data (Jullien, 2023) are shown in orange for reference. For each mosaic, the zoom-in panels show details of the North Greenland ice slab region. e) North Greenland σ^0_{HV}. f) North Greenland σ^0_{xpol}. g) North Greenland $\Delta\sigma^0$. h) North Greenland OIB ice slab detections. In all panels, the Greenland coastline was produced by the British Antarctic Survey (Gerrish, 2020), the ice mask as part of BedMachine v3 (Morlighem et al., 2017), and the 200 m contours are derived from ArcticDEM (Porter et al., 2018). (Note: Panels a-c contain modified Copernicus Sentinel data 2016-2017, originally processed by ESA.)

zone, this occurs because the subsurface is dominated by smooth depositional snow layers with little heterogeneity beyond the ice grain scale. Firn aquifer regions retain liquid meltwater through the winter which leads to increased subsurface absorption and therefore a relatively greater degree of surface scattering, since subsurface volume scattering is suppressed (Brangers et al., 2020; Miller et al., 2022a).

To exclude regions with minimal surface melting, we adapt an existing method for mapping wet snow facies in Greenland based on the change in S-1 σ^0_{HH} between winter and summer (Hu et al., 2022). Much like the classic ~~scatterometer and~~ radar scatterometer and microwave radiometer algorithms for mapping surface melting and firn saturation from VV backscatter (Wismann, 2000; Ashcraft and Long, 2006; Hicks and Long, 2011; Miller et al., 2022b), this approach exploits the fact that the enhanced microwave absorption in wet snow leads to a significant reduction in backscatter during the summer when surface melting occurs. We first ~~calculate~~ create an average winter σ^0_{HH} map at 35° incidence angle by applying the same linear correction method described in Section 3.1 to aggregated data from 1 Nov - 31 March each year between 2014 and 2020. We ~~calculate~~ then create an average summer σ^0_{HH} map ~~at 35°~~ using all observations between 1 July and 31 Aug from 2015-2020~~and then~~, corrected to 35° in the same manner. Finally, we calculate the difference between the summer and winter backscatter as $\Delta\sigma^0 = \sigma^0_{summer} - \sigma^0_{winter}$. We aggregate data over these five years because melt extent varies significantly from year to year and from region to region. This extended time series prevents us from inadvertently excluding areas from analysis due to anomalously low melt extent in any given year~~.~~, despite a sufficient history of melt to have formed ice slabs. Additionally, it ensures we have sufficient observations with sufficient angular diversity during the three month summer period. We then choose an empirical threshold to discriminate regions with consistent surface melting. Hu et al. (2022) derived a threshold of -7 dB to discriminate between wet snow facies and the percolation zone in ~~the~~ $\Delta\sigma^0$ ~~image~~images, based on the distribution of backscatter values observed in Northeast Greenland. However, we find that this threshold is overly aggressive when applied to our average $\Delta\sigma^0$ map and excludes some regions in North Greenland where ice slabs have been observed with ice-penetrating radar. Therefore, we use a threshold of $\Delta\sigma^0 <$ -4.7 dB, which is the minimum value that produces a melt region mask which encompasses all OIB ice slab observations from spring 2017. This threshold value falls midway between the Hu et al. (2022) threshold of -7 dB for discriminating wet snow facies and the common threshold of -3 dB for discriminating regions of surface melting (Nagler and Rott, 2000; Liang et al., 2021; Li et al., 2023), suggesting that this is a reasonable empirical choice that is consistent with prior work on wet snow mapping with S-1. Figure 2c shows the five-year melt extent mosaic, with the region we consider for ice slab detection ($\Delta\sigma^0 <$ -4.7 dB) highlighted in the blue.

To exclude firn aquifer regions, we use the Sentinel-1 firn aquifer map originally published in Brangers et al. (2020). These firn aquifer areas were detected by identifying pixels where the mean April σ^0_{HV} exceeded the mean September σ^0_{HV} by 9.4 dB or more, using mean monthly values aggregated over 2014-2019, similar to our ~~firn saturation~~ melt area map. Figure 2d shows the locations of these firn aquifers in relation to previous OIB ice slab detections.

3.3 Threshold Optimization and Uncertainty Analysis

~~To map ice slabs with our~~ Sections 3.1 and 3.2 describe how we form σ^0_{xpol} and σ^0_{HV} mosaics over high-melt regions where ice slab formation might be possible. To then map ice slab extent, we choose backscatter thresholds that can delineate regions with ice slabs from regions without ice slabs. We assess uncertainty by quantifying the range of plausible S-1 ~~mosaics, we optimize independent~~ inferred ice slab extents that would be consistent with the OIB airborne ice-penetrating radar observations. We approach this problem in two steps. First, we use all available OIB ice slab detections to find the optimal backscatter thresholds that ~~demarcate the upper and lower limit of the ice slabs. For the upper boundary, we first take the σ^0_{HV} and σ^0_{xpol} mosaics and mask out the dry snow zone and firn aquifer regions. We then define ice slabs as covering the region where $\sigma^0_{HV} < \alpha$ and $\sigma^0_{xpol} < \beta$, where α and β are independent empirical thresholds. We search for the optimal values of α and β that maximize the~~ produce the best ice-sheet-wide agreement between the ~~upper limit of the ice slabs as detected by airborne ice-penetrating radar~~S-1 inferred ice slab extent and the OIB ice slab extent. By applying these optimal thresholds to the backscatter mosaics,

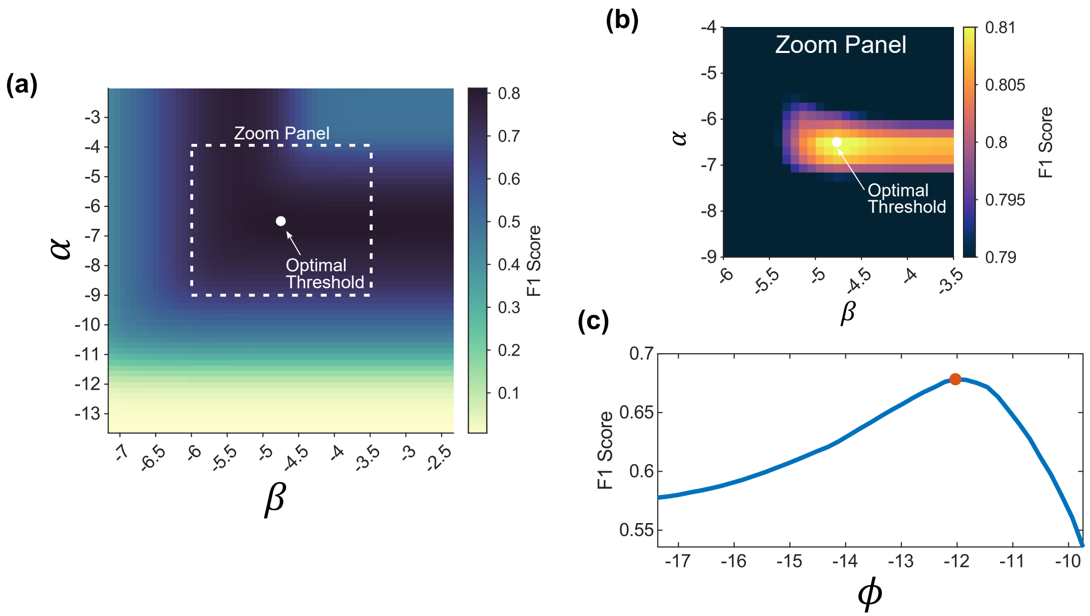

Figure 3. ~~Optimization~~ Selection of the ~~detection~~ optimal thresholds for ~~the upper limit of~~ ice ~~slabs~~slab detection. a) F1 score for delineating the upper elevation limit of the ice slabs as a function of ~~σ^0_{xpol}~~ α and ~~σ^0_{HV}~~ β thresholds. The optimal threshold combination (maximum F1 score) is shown in the white dot. b) ~~Optimal thresholds from each iteration~~ Zoom-in of the ~~ten-fold cross validation scheme. The thresholds that give~~ region around the ~~minimum and~~ optimal threshold combination, showing the global maximum ~~total ice slab extent are marked~~ in ~~the grey bars~~F1 score. ~~We use these two thresholds to quantify uncertainty in the upper limit of the ice slabs.~~ c) ~~The total ice slab area and~~ F1 score ~~on the withheld validation set~~ for ~~each iteration of~~ delineating the lower elevation limit of the ice slabs as a function of φ threshold. The optimal threshold (maximum F1 score) is shown in the red dot.~~ten-fold cross-validation.~~

we produce a map of the most likely ice slab extent across the ice sheet. Then, to assess uncertainty, we use a 10-fold cross validation scheme where we generate 10 new sets of thresholds, each optimized using only a small subset of the OIB data. From the results of these ten trials, we use the backscatter thresholds that produce the largest total ice slab area to define the maximum plausible ice slab extent, and the ~~upper limit of the ice slabs as estimated by~~ thresholds that produce smallest total ice slab area to define the minimum plausible ice slab extent. Together, this quantifies the range of plausible S-1 ~~.~~ inferred ice slab extents that are still a good fit to the OIB observations. Below, we describe in detail how we choose these thresholds.

~~To optimize α and β, we create~~

3.3.1 Most Likely Ice Slab Extent

We use a training data set ~~using the Jullien et al. (2023)~~ built from the Jullien et al. (2023) high-end estimate of ice slab extent derived from OIB flight lines surveyed in March-May 2017. (This high-end estimate corresponds to the maximum likely refrozen ice content given the observed ice-penetrating radar signal strength.) For each flight line that passes through an ice

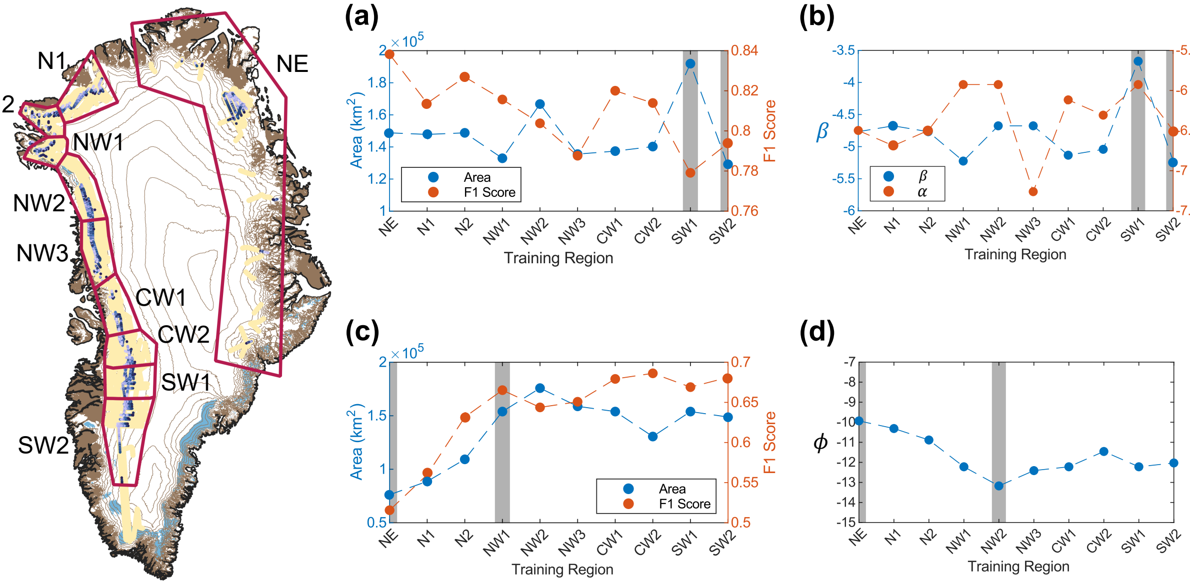

Figure 4. Results of the ~~ten-fold cross validation~~ 10-fold cross-validation scheme. The ~~thresholds~~ overview map of Greenland shows the ten training regions. In each panel, The training regions that ~~give~~ produce the maximum and minimum total ice slab extent are marked in the grey bars. ~~We use these two thresholds to quantify uncertainty in~~ a) The total ice slab area and F1 score on the ~~lower limit~~ withheld validation set for each iteration of the ten-fold cross-validation of the ice ~~slabs~~slab upper elevation limit. b) The estimated values of α and β derived from each of the ten training regions. c) The total ice slab area and F1 score on the withheld validation set for each iteration of the ten-fold cross-validation ~~. We discard~~ of the ~~iteration marked with the red bar to due to the anomalously poor F1 score and choose the maximum and minimum~~ ice slab ~~extents~~ lower elevation limit. d) The estimated values of ϕ derived from each of the ~~remaining nine iterations (marked in the two gray bars)~~ten training regions.

slab area, we extract the portion of the flight line that overflies the ice slabs, as well as an additional 50 km buffer that extends inland of the upper limit of the ice slabs. We discretize these lines into points every 50 m and assign each point a value of 1 if an ice slab was detected in the OIB data at that location or 0 if no ice slab was detected. ~~Similarly, we binarize our S-1 ice slab detections where a pixel value of 1 means an ice slab was detected~~ These observations are then used to optimize the backscatter thresholds. We use a brute force search to find optimal values of α and ~~0 means no ice slab was detected.~~ β that maximize the agreement between the upper elevation limit of the ice slabs as detected by airborne ice-penetrating radar, and the upper limit of the ice slabs as estimated by S-1. Areas where $\sigma^0_{HV} < \alpha$ and $\sigma^0_{xpol} < \beta$ are taken to be ice slabs. We then test all combinations of thresholds ~~for -7.12 dB $< \beta <$ -2.37 dB and~~ where -13.6 dB ~~$< \alpha <$ -2.1~~ $< \alpha <$-2.1 dB and -7.12 dB $< \beta <$ -2.37 dB, calculate the F1 score for each combination, and choose the threshold values that give the highest F1 score. The F1 score is a measure of the accuracy of a binary classification and is calculated following Equation 1.

$$\mathrm{F1} = \frac{2 * \text{true positive}}{2 * \text{true positive} + \text{false positive} + \text{false negative}} \tag{1}$$

Figure 3 shows this optimization trade space~~with the optimal threshold combination shown in the white dot~~. We find that using both σ^0_{xpol} and σ^0_{HV} thresholds together leads to modestly better agreement with the OIB detections, compared to using only σ^0_{xpol}. ~~The optimal ice slab extent estimated using~~ When only σ^0_{xpol} ~~has an~~ is used to delineate the upper elevation limit of the ice slabs, this F1 score ~~of~~ is 0.787, compared to an F1 score of 0.811 ~~for the joint optimization. The optimal ice slab extent estimated~~ when both backscatter thresholds are used. When using only σ^0_{HV} ~~has an~~ to delineate the upper elevation limit of the ice slabs, the F1 score ~~of~~ is only 0.674, so it is clear that ~~the cross-polarized backscatter ratio provides significant additional information .~~

$$\mathrm{F1} = \frac{2 * \text{true positive}}{2 * \text{true positive} + \text{false positive} + \text{false negative}}$$

σ^0_{xpol} provides additional information that improves the delineation of the upper boundary.

~~To quantify uncertainty in our detection of the upper~~ Initial analysis of the backscatter mosaics suggests that σ^0_{xpol} does not display an unique change in behavior associated with the lower boundary (see Figure 2), so we optimize a separate threshold, $\sigma^0_{HV} > \phi$, to delineate the lower elevation limit of the ice slabs~~,~~. We optimize ϕ following the same method as described above, but using a new version of the OIB training dataset that covers the ice slab region and a 50 km buffer down-flow into the ablation zone. Altogether, the area defined by $\sigma^0_{xpol} < \beta$ and $\phi < \sigma^0_{HV} < \alpha$ is our most likely estimate of the spatial extent of ice slabs across the ice sheet.

3.3.2 Maximum and Minimum Ice Slab Extent

To quantify uncertainty in this most likely estimate of ice slab extent, we use a ~~ten-fold cross-validation~~ 10-fold cross validation scheme. We divide our training dataset into ~~ten even subsets, rerun our optimization routine on each data subset, and~~ 10 subsets, each containing OIB ice slab detections from a different region of the ice sheet (see Figure 4). For each of the ten regions, we again use a brute force search to find the values of α, β, and ϕ that produce the best agreement between the OIB ice slab detections and S-1 inferred ice slab extent in that region. We then apply those local thresholds to the entire ice sheet and calculate the F1 score ~~on the~~ by comparing the S-1 ice slab mapping to the $\sim$90% of the ~~data that was withheld. This yields ten separate estimates of the optimal backscatter thresholds, tuned to different regions~~ OIB observations that were not used to choose α, β, and ϕ in that trial. As with the most likely ice slab extent, we calculate separate F1 scores for the upper and lower limits of the ice ~~sheet. We take the thresholds that yield the maximum and minimum~~ slabs. From the results of these ten trials, we use the backscatter thresholds that produce the largest total ice slab area ~~and use these limits to bound the plausible extent of the ice slabs as estimated by S-1~~to define the maximum plausible ice slab extent, and the thresholds that produce smallest total ice slab area to define the minimum plausible ice slab extent. Figure ~~3c-d shows the result of this analysis.~~

~~Next we separately optimize the threshold for detecting the lower boundary~~ 4 shows the results of this cross-validation. We find that across the 10 validation trials, F1 scores for the upper elevation limit of the ice slabs ~~using the same method as~~

~~described above, but now using a training dataset that covers the ice slab region and a 50 km buffer down-flow into the ablation zone. Initial analysis of the backscatter mosaics suggests that σ^0_{xpol} does not display any distinct change in behavior associated with the lower boundary (see Figure 1a), so we optimize a single threshold, $\sigma^0_{HV} > \phi$, with uncertainty determined using the same ten-fold cross-validation scheme described above.~~ vary from 0.78-0.84, with no clear spatial trend. Since the F1 score for the most likely ice slab extent is 0.811, this suggest that values of α and β chosen based on data from one region of the ice sheet generalize well to other regions. Indeed, these thresholds vary by only $\sim \pm$ 1 dB across all regions of the ice sheet. Therefore, we assess that the algorithm is reasonably spatially robust.

~~Finally, we use our optimized thresholds to map the minimum, most likely, and maximum extent of ice slabs from~~ We do find a clear spatial trend in the generalizability of ϕ between regions. In particular, when ϕ is derived only using data from regions NE and N1, the resulting S-1 inferred ice slab extent in Northwest and Southwest Greenland agrees poorly with the ~~S-1 data following the complete workflow shown in Figure 5. To quantify the accuracy of these mapped extents, we calculate the confusion matrix, F1 score, and Cohen's κ for each limit~~OIB observations. Conversely, the value of ϕ estimated using only data from the Northwest and Southwest does apply well to the North and Northeast. We suggest three explanations for this behavior. First, the North and Northeast regions have the least number of ice slab detections, so thresholds derived from data in those regions may be overfit to conditions that are not representative of larger areas. Second, snow accumulation in the North and Northeast is significantly lower than in other parts of teh ice sheet, potentially leading to difference in ice slab structure and overlying snow cover. Third, we see steeper gradients in backscatter as a function of elevation in the North compared to the Northwest and Southwest. This suggests that small variations in ϕ would lead to large changes in ice slab area in the Northwest and Southwest, but small changes in ice slab area in the North and Northeast. As a result, the agreement between the OIB observations and S-1 detections is much more sensitive to errors in ϕ in the Northwest and Southwest than in the North and Northeast.

4 Results and Discussion

4.1 Sentinel-1 Map of Ice Slab Extent

Figure 6 shows the S-1 estimated ice slab extent in winter 2016-2017, compared with the OIB ice slab detections. We find ~~excellent~~ good agreement between the upper limit of the ice slabs as identified by OIB and the S-1 estimated upper limit. Figure 7 shows the confusion matrices, F1 scores, and Cohen's κ for the minimum, most likely, and maximum S-1 estimated ice slab extent that quantify this agreement. The most likely ice slab extent has an F1 score of 0.811 with a true positive rate of 94% when detecting the upper limit of the ice slabs. However, it is important to keep in mind that the optimal values of α, β, and ϕ are derived from all available ice-penetrating radar detections. Therefore, the high F1 score quantifying the agreement between the OIB detections and most likely ice slab extent mapped by S-1 simply indicates that there is a sufficiently unique relation between S-1 backscatter and firn shallow ice content that S-1 backscatter can reasonably be used as a proxy to map ice slabs. The high F1 score does not provide information on whether α, β, and ϕ generalize to data collected in other places or at other times. However, the 10-fold cross validation scheme estimates α, β, and ϕ using only $\sim$10% of the OIB data and

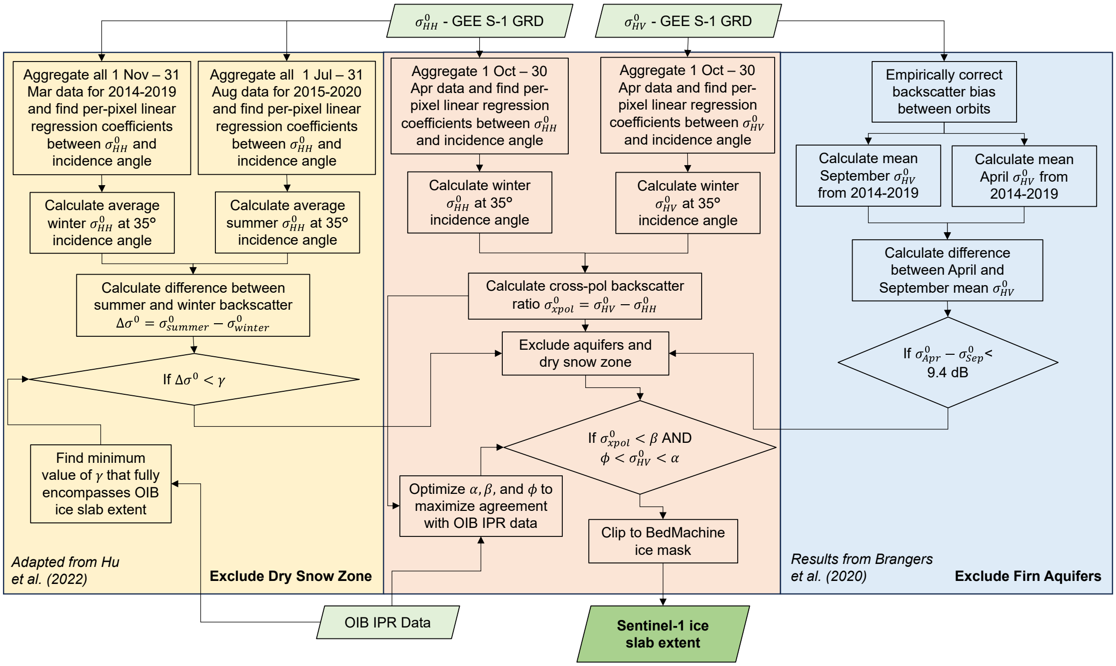

Figure 5. Sentinel-1 ice slab detection algorithm flowchart.

validates the applicability of that threshold to the rest of the ice sheet using the withheld ∼90% of the data. Therefore, the minimum and maximum ice slab extents, derived from this cross-validation scheme, show how well thresholds estimated in one region of the ice sheet can be generalized to the ice sheet as whole.

The S-1 estimates at 500 m are ~~also~~ able to capture much of the km-scale variability along the upper ~~limit~~elevation limit of the ice slabs, including regions of discontinuous ice slabs (see Figure 6f for an example). The fingering structures that we map in many regions are consistent with preferential expansion through topographic lows where water collects as it flows laterally through saturated firn layers.

~~Our mapping~~ Our mapping also identifies new ice slab regions in Southwest Greenland that have not been previously classified as such, likely due to a lack of comprehensive airborne radar coverage in this region. These newly-identified ice slab areas are highly consistent with the extent of the visible runoff zone mapped from Landsat imagery in Tedstone and Machguth (2022), confirming that vertical percolation is limited in these areas (Figure 8). They are also consistent with recent firn model estimates of ice slab extent in this region (Brils et al., 2024). However, the S-1 ice slab extent is often patchy and discontinuous in this region, likely due to the high prevalence of buried surface lakes and isolated aquifer regions that limit detection of ice slabs due to the presence of liquid water in the subsurface.

There are also a number of discrepancies between the OIB and S-1 mapping. In the northwest, S-1 appears to slightly underestimate the upper elevation limit of the ice slabs, particularly ~~where they transition to firn aquifers~~in the northern portion

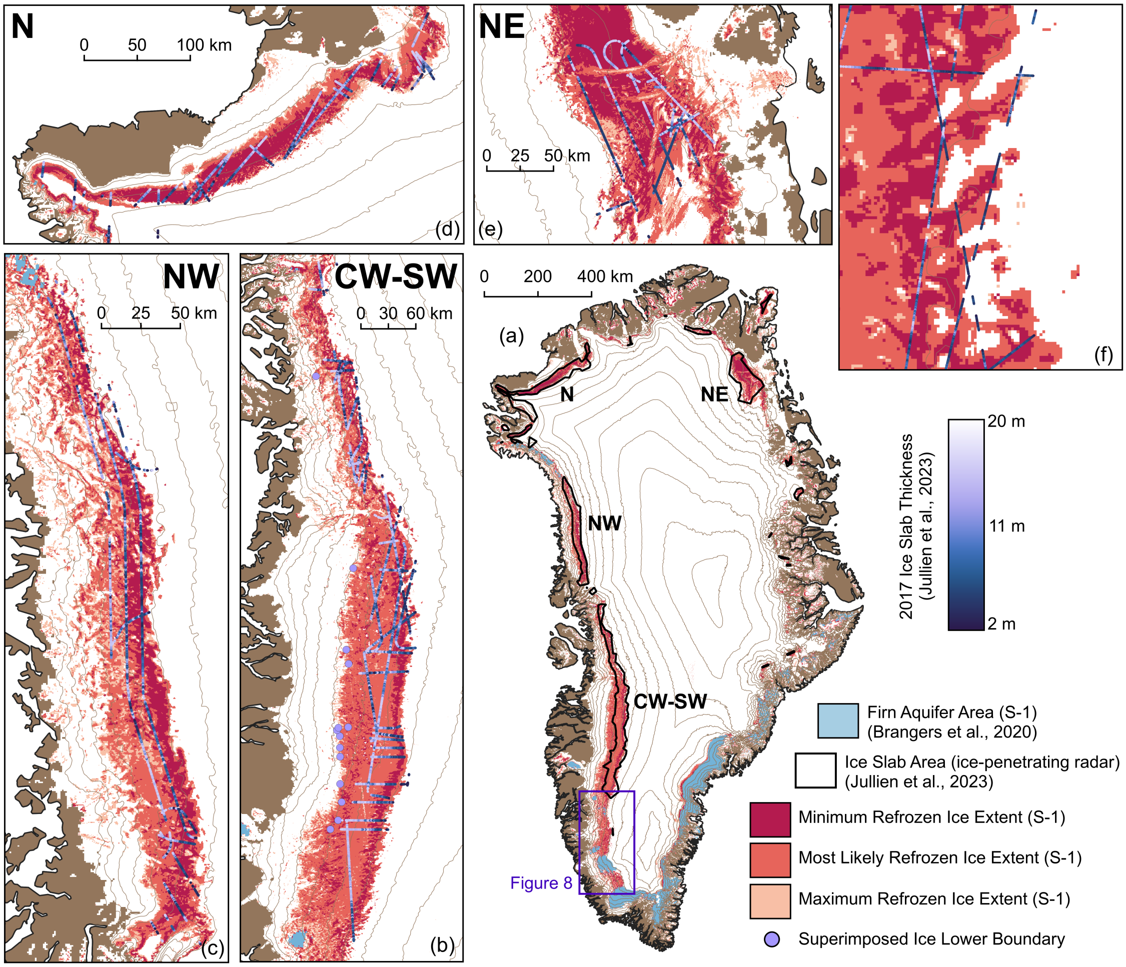

Figure 6. Sentinel-1 mapping of ice slabs in winter 2016-2017. a) S-1 detected ice slabs are shown in red, with the outline of the OIB detected ice slabs in the ~~dashed~~ black line (Jullien, 2023). We find overall ~~excellent~~ strong agreement between the S-1 and OIB mapping, although S-1 detects significant additional ice slab area in Southwest Greenland, along the Central East margin, and on peripheral ice caps. b) Zoom-in of the Central and Southwest regions. OIB ice slab detections are overlaid in the purple dots (Jullien, 2023), where darker colors indicated thinner ice slabs. There is a significant gap between the lower limit of the OIB ice slab detections and the lower limit of the S-1 mapping. The lower limit from S-1 is better aligned with the lower limit of superimposed ice as mapped from ice-penetrating radar in this paper (large purple dots). c) Zoom-in of Northwest region. d) Zoom-in of Northern region. e) Zoom-in of Northeast region. f) Zoom-in from Southwest Greenland showing details of the upper boundary. We find ~~excellent~~ good agreement between the OIB and S-1 detections even where ice slabs are discontinuous due to preferential expansion in topographic lows. In all panels, the Greenland coastline was produced by the British Antarctic Survey (Gerrish, 2020), the ice mask as part of BedMachine v3 (Morlighem et al., 2017), and the 200 m contours are derived from ArcticDEM (Porter et al., 2018).

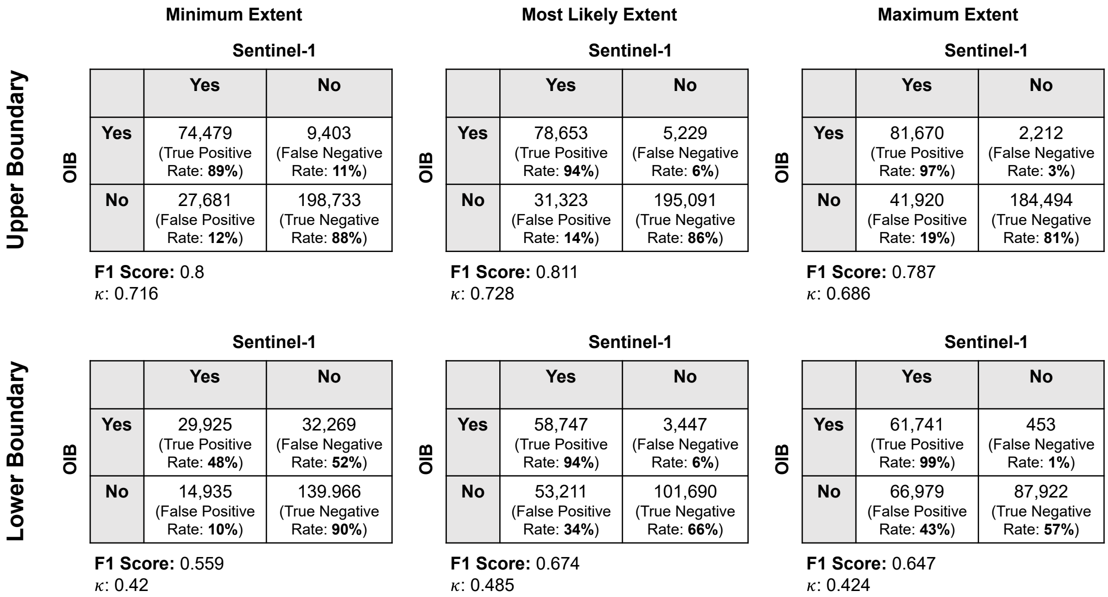

Upper Boundary

Minimum Extent

Sentinel-1

OIB	**Yes**	**No**
Yes	74,479 (True Positive Rate: **89%**)	9,403 (False Negative Rate: **11%**)
No	27,681 (False Positive Rate: **12%**)	198,733 (True Negative Rate: **88%**)

F1 Score: 0.8
κ: 0.716

Most Likely Extent

Sentinel-1

OIB	**Yes**	**No**
Yes	78,653 (True Positive Rate: **94%**)	5,229 (False Negative Rate: **6%**)
No	31,323 (False Positive Rate: **14%**)	195,091 (True Negative Rate: **86%**)

F1 Score: 0.811
κ: 0.728

Maximum Extent

Sentinel-1

OIB	**Yes**	**No**
Yes	81,670 (True Positive Rate: **97%**)	2,212 (False Negative Rate: **3%**)
No	41,920 (False Positive Rate: **19%**)	184,494 (True Negative Rate: **81%**)

F1 Score: 0.787
κ: 0.686

Lower Boundary

Sentinel-1

OIB	**Yes**	**No**
Yes	29,925 (True Positive Rate: **48%**)	32,269 (False Negative Rate: **52%**)
No	14,935 (False Positive Rate: **10%**)	139.966 (True Negative Rate: **90%**)

F1 Score: 0.559
κ: 0.42

Sentinel-1

OIB	**Yes**	**No**
Yes	58,747 (True Positive Rate: **94%**)	3,447 (False Negative Rate: **6%**)
No	53,211 (False Positive Rate: **34%**)	101,690 (True Negative Rate: **66%**)

F1 Score: 0.674
κ: 0.485

Sentinel-1

OIB	**Yes**	**No**
Yes	61,741 (True Positive Rate: **99%**)	453 (False Negative Rate: **1%**)
No	66,979 (False Positive Rate: **43%**)	87,922 (True Negative Rate: **57%**)

F1 Score: 0.647
κ: 0.424

Figure 7. Confusion matrices quantifying the agreement between the OIB and S-1 ice slab detections for the minimum, maximum, and most likely ice slab extents. We quantify the fit for the upper boundary (top row) and lower boundary (bottom row) separately, since these thresholds were optimized separately. The most likely extent does an excellent job of detecting the upper limit of the ice slabs, with an F1 score of 0.811 and Cohen's κ of 0.727, but the lower boundary is much more uncertain, with a best F1 score of only 0.674 and Cohen's κ of 0.485, likely due to the consistent overestimation of ice slab extent in Southwest Greenland.

of this region, and the ice slab extent is fairly discontinuous in this ~~region~~area. The S-1 algorithm generally fails to detect ice slabs in basins with persistent buried supraglacial lakes because surface scattering from the water table dominates the return, likely contributing to this discontinuous mapping in the Northwest where buried lakes are common ~~(Koenig et al., 2015)~~ (Koenig et al., 2015; Dunmire et al., 2021). In the Northeast, the S-1 algorithm fails to detect gaps in the ice slabs in the shear margins of the Northeast Greenland Ice Stream that are present in the OIB data. This highlights that regions with significant surface crevassing are challenging for both OIB and S-1 detection of ice slabs. S-1 will tend to overestimate ice slab extent in crevassed regions, due to enhanced σ^0_{HV} that our algorithm ascribes to volume scattering from firn, but actually results from rough surface and multi-bounce effects within the crevasses. On the other hand, surface crevasse clutter in the OIB data can prevent definitive classification of the near-surface structure, particularly when using radiometric metrics that assume relatively homogeneous planar structures. The S-1 algorithm also fails to detect some isolated ice slab segments identified at anomalously high elevations in the OIB data in the North and Northwest. Manual review of the radargrams in these areas shows that most fall in high melt, high accumulation areas where a thick layer of relatively transparent winter snow overlying a strong reflector at the previous summer surface may have been misclassified as an ice slab.

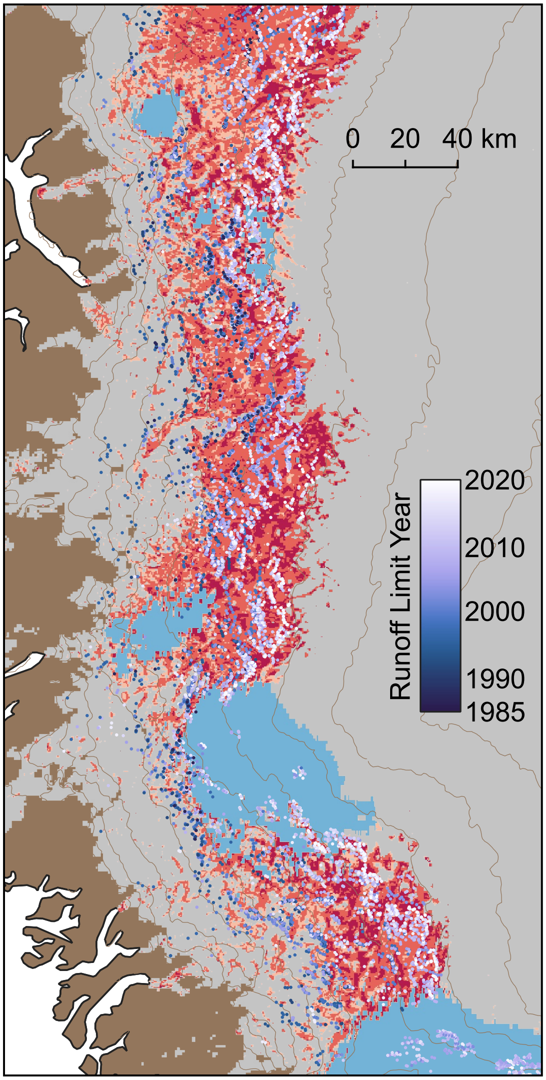

Figure 8. Comparison of the maximum visible runoff line from 1985-2020 with the newly mapped ice slabs regions in Southwest Greenland. The ice slab regions are marked with the same orange and red color scheme as Figure 6 and firn aquifers are shown in light blue (Brangers et al., 2020). Points marking the visible runoff limit in each sector, color-coded by year of observation, are overlaid in purple (Tedstone, 2022). There is a clear correspondence between the newly mapped ice slab regions and the runoff limit, confirming that vertical percolation is limited in these areas. The Greenland coastline was produced by the British Antarctic Survey (Gerrish, 2020), the ice mask as part of BedMachine v3 (Morlighem et al., 2017), and the 200 m contours are derived from ArcticDEM (Porter et al., 2018).

We also consistently map ice slabs along the upper boundaries of firn aquifer, both in the Northwest and Southeast, that are not identified in the OIB data. It is possible that these areas represent aquifer regions with low volumetric water content where the seasonal backscatter variability does not meet the threshold for aquifer detection, but surface scattering at the upper surface of the aquifer is still enhanced by partial winter meltwater retention. Time series of σ^0_{HV} from these aquifer-marginal areas in the Southeast show an intermediate scattering regime, with slower backscatter recovery than the percolation zone, but more rapid recovery than the well-defined aquifer regions. Alternately, there is ice-penetrating radar evidence for near-surface refreezing in continuous ice layers less than 1 m thick following both the 2012 and 2015 melt seasons (Culberg et al., 2021; Miller et al., 2022a) that extend to the upper limit of the southeastern firn aquifers. Similar shallow ice layers might also contribute to enhanced surface scattering and lead to erroneous ice slab detections in the Southeast.

Overall, we estimate a most likely ice slab extent of 104,020 km^2, compared to previous estimates of 60,400 - 73,500 km^2 from OIB data processed in Jullien et al. (2023)~~and~~ , 76,000 km^2 from SMAP data processed in Miller et al. (2022a), and 230,00 km^2 from firn modeling (Brils et al., 2024). Much of this additional area comes from the newly detected regions in Southwest Greenland, as well as smaller contributions from narrow regions along the periphery, peripheral ice caps including Flade Isblink, and some misclassified regions at lower elevations and in fast-flowing glacier tongues in the mountainous eastern basins. Difficulty in accurately mapping the lower boundary of the ice slabs, further discussed in Section 4.2, also adds to the discrepancy in total extent.

4.2 Uncertainty in the Lower Boundary of Ice Slabs

Mapping the lower elevation limit of ice slabs is significantly more challenging than mapping the upper limit, as evidenced by the large uncertainty and apparently poor fit with the OIB detections. Our best estimate of the lower limit of the ice slabs has an F1 score of 0.674, compared to 0.811 for the upper boundary (Figure 7). There are ~~two~~ three major sources of uncertainty which may contribute to this poor fit. First, it is likely that the limited penetration depth of S-1 prevents a clear delineation between regions where ice slabs are simply thicker than the system depth sensitivity and regions with a solid ice column. Figure 9 shows two-dimensional histograms of S-1 backscatter versus OIB-detected ice slab thickness. Both σ^0_{HV} and σ^0_{xpol} show little to no relationship with ice slab thickness beyond $\sim$7 m, suggesting that S-1 is largely insensitive to scattering structure below that depth. Since well-developed ice slabs in regions such as Southwest Greenland are often 8-10 m thick, it is unsurprising that S-1 struggles to clearly detect the transition from ice slabs to solid ice. Second, the lower limit of the ice slabs in the airborne ice-penetrating radar dataset is not actually a data-driven boundary. Jullien et al. (2023) used the RACMOv2.3p regional climate model to exclude any regions below the long-term equilibrium line from their analysis, so the lower boundary is actually set by the model results. Given the simple snow model coupled to RACMO, the model may not accurately capture the true extent of ice slabs. ~~edAdditionally, it almost certainly does not capture complex regions where near-surface ice may have been~~ Finally, there are likely regions within the upper ablation zone and lower equilibrium zone which do not meet the formal definition of ice slabs, but where surface ice was still formed by refreezing ~~, even if firn is no longer present. This includes historical ice slab regions , superimposed iceregions~~rather than compaction. These may include regions of superimposed ice, where meltwater fully saturates the annual accumulation and refreezes to form surface ice layers (Benson, 1962), areas where the ~~firn column may have~~ relict firn layer has been completely filled by surface meltwater draining through surface crevasses (Culberg et al., 2022a), or regions where refrozen ice was advected in from older ice slabs that formed at higher elevations. These areas would typically not be classified as ice slabs, since they lack a deep layer of relict porous firn beneath the ice at the surface. However,

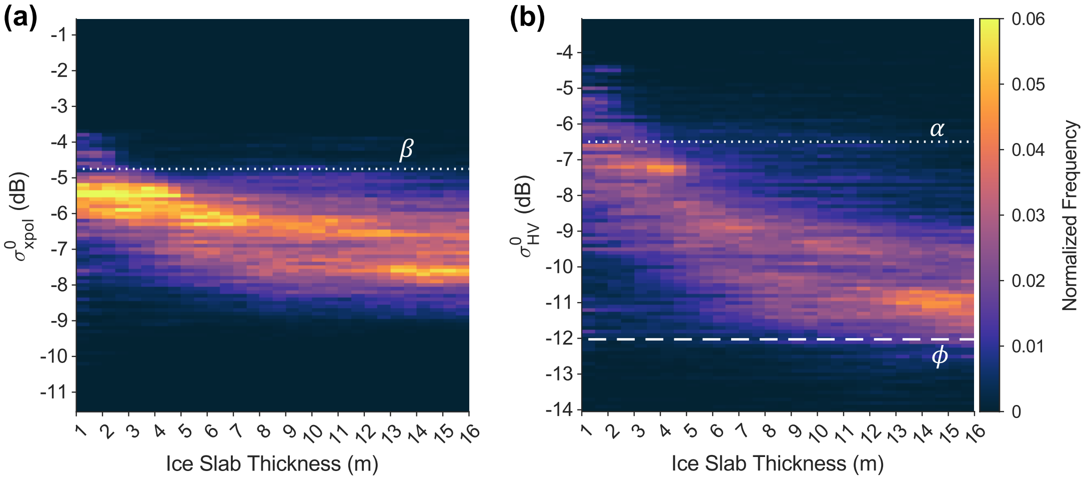

Figure 9. Sentinel-1 backscatter sensitivity to subsurface structure. a) Normalized two-dimensional histogram of ice slab thickness from ice-penetrating radar versus ~~Sentinel-1~~ S-1 σ^0_{xpol}. b) Normalized two-dimensional histogram of ice slab thickness from ice-penetrating radar versus ~~Sentinel-1~~ S-1 σ^0_{HV}. In both cases, the change in backscatter saturates around an ice slab thickness of $\sim$ 7 m, suggesting that the S-1 penetration depth is limited to approximately that depth. The optimal thresholds for the upper and lower limit of the ice slabs are shown in dashed white lines on each plot. This figure also demonstrates that the σ^0_{xpol} metric improves detection of the ice slab upper limit because the spread of backscatter values that map to an ice slab thickness of 1-2 m is significantly reduced compared to σ^0_{HV}.

since the surface ice was formed by refreezing, the C-band backscatter signatures are likely more similar to ice slabs than to regions of the ablation zone where the surface consists of meteoric ice exhumed by ablation.

~~We~~ Specifically, we hypothesize that any ice formed by refreezing induces ~~significant~~ notable volume scattering due to trapped ~~air bubbles,~~ interstitial firn pockets ~~,~~ and other heterogeneities in density, leading to a σ^0_{HV} signature that is more similar to ice slabs than meteoric ice. This is consistent with previous work which ~~showed~~ has shown clear differences in C-band polarimetric backscatter between glacier ice, superimposed ice, and firn regions (Langley et al., 2008, 2009; Barzycka et al., 2019). To test this hypothesis, we reanalyze 14 airborne radar data flights from 2017 in Central West and Southwest Greenland that are approximately parallel to ice flow. Both the IMAU Firn Densification model (Brils et al., 2022) and the maximum depth of ice blobs observed in the Jakobshavn catchment (Culberg et al., 2022a) suggest that pore close-off occurs at around 30 m depth in this region. Therefore, in each radargram, we identify an englacial layer that is approximately 30 m below the surface near the upper limit of the ice slabs and assume it represents the bottom of the firn column. We trace this layer downstream until it outcrops at the surface due to ablation. Where surface sidelobes obscure the radiostratigraphy or there are significant stratigraphic disturbances near the surface, we estimate the maximum outcropping elevation as the last point where the layer can be clearly traced, and the minimum elevation as the point where we would extrapolate the layer outcropping to occur if the layer slope remained the same. Figure 10a shows an example of this layer tracing process. We infer that ice at depths shallower than the traced layer was likely formed by refreezing, rather than compaction.

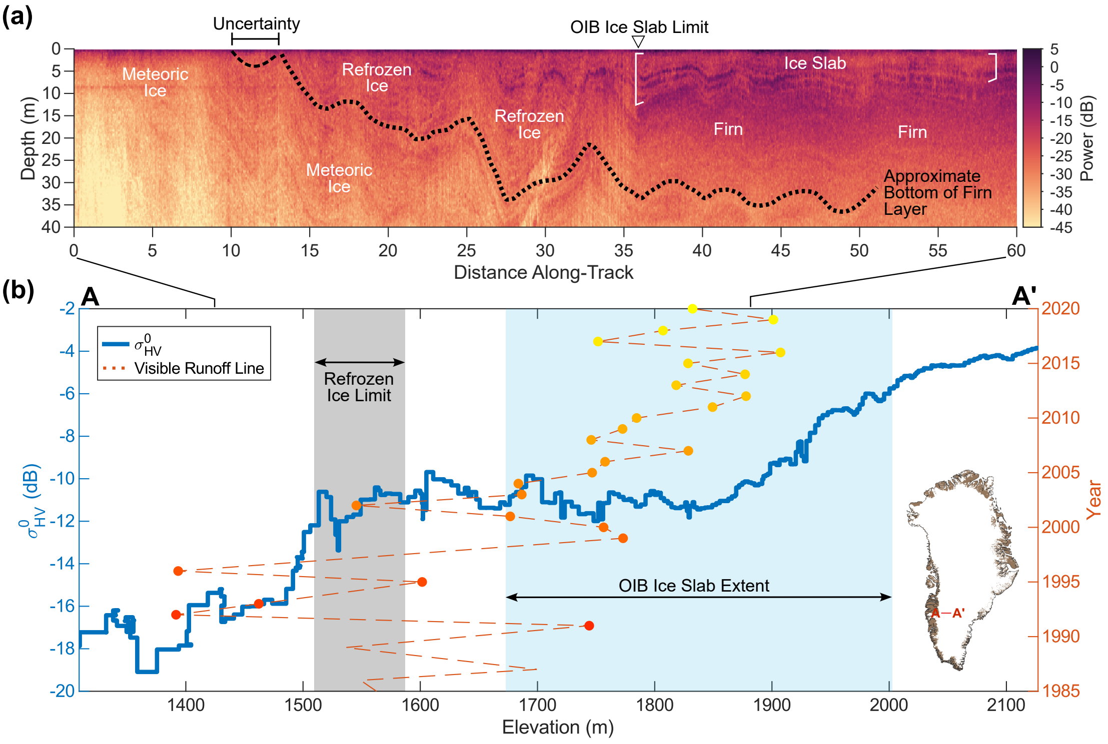

Figure 10. Sentinel-1 detects the lower limit of ~~refrozen~~ superimposed ice facies. ~~(Contains modified Copernicus Sentinel data 2016-2017, processed by ESA.)~~ a) Accumulation Radar transect from April 2017 (Paden et al., 2014b) showing the inferred transition from ice slabs, to superimposed ice facies, to solid meteoric ice. The dashed black line shows the englacial layer that we trace from the bottom of the firn until it outcrops at the surface in order to define the lower limit of the ~~refrozen~~ superimposed ice facies. b) Comparison of σ^0_{HV} (blue line) as a function of elevation with the OIB ice slab extent (blue patch) (Jullien, 2023), estimated lower boundary of superimposed ice facies (grey patch, this paper), and the elevation of the visible runoff line between 1985 and 2020 (dashed red line with dots at annual measurement points) (Tedstone, 2022). The region where we infer that surface ice was formed by refreezing is marked by a plateau in σ^0_{HV} around -11 dB and is also the region over which the visible runoff zone has retreated in the last two decades, supporting the idea that this region may have been near or above the firn-line in the recent past. The inset map in panel b (Gerrish, 2020; Morlighem et al., 2017) shows the location of this transect in Southwest Greenland. (Contains modified Copernicus Sentinel data 2016-2017, processed by ESA.)

In Figure 6b, the large purple dots mark the minimum elevations of these outcropping points, showing strong agreement between the S-1 inferred lower boundary of ice slabs and this new OIB-inferred limit of ~~refrozen surface~~ superimposed ice facies. This region between the boundary of ~~refrozen~~ the superimposed ice facies and the lower limit of the OIB-mapped ice slabs corresponds to the area over which the visible runoff line has retreated since the mid-1980s (see Figure 10) (Tedstone and Machguth, 2022), with significant interannual variability in runoff extent. This suggests that the S-1 mapping in part captures the historical equilibrium zone, which would have been in positive mass balance prior to the 1980s and may have still experienced intermittent years of positive mass balance into the early 1990s. Given the slow ice flow in the Southwest (∼40 $\mathrm{ma^{-1}}$), this contributes to a wide zone where surface ice consists of ~~historical~~ old ice slabs that have not yet fully ablated, further modified by intermittent superimposed ice formation, and ongoing downstream advection of ~~other refrozen ice~~ newer ice slabs. Therefore, we infer that our S-1 mapping captures not only ice slabs, but all regions where the near-surface ice was formed predominantly by refreezing.

This conclusion is consistent with some of the regional differences in the mismatch between the S-1 and OIB-inferred lower extent of the ice slabs. In the Southwest, there is a 20-35 km gap between the bottom of the OIB-detected ice slabs and S-1 mapped ice slabs. This is consistent with the low surface slopes, long history of melt, and slow and variable retreat of the snowline and expansion of the visible runoff zone in this region (Ryan et al., 2019; Tedstone and Machguth, 2022). In contrast, the two mappings agree fairly well in the North which has seen more consistent expansion of the runoff zone and retreat of the snowline since 1990 (Ryan et al., 2019; Noël et al., 2019), suggesting that the formation of ~~refrozen~~ extensive superimposed ice facies in this region is a more recent and rapid phenomenon. However, some of the discrepancies in the lower limit are likely attributable to other complex surface scattering mechanisms rather than an extended superimposed ice zone. For example, in the Northwest, the S-1 lower limit is particularly diffuse, with complicated and disconnected regions identified as potential refrozen ice all the way to the ice sheet margin. We hypothesize that this is due to a propensity for regions of heavy crevasses to be misclassified as refrozen ice, an issue which is more pronounced in the fast-flowing Northwest where surface strain rates are high and crevassing is prevalent.

4.3 Comparison with ~~SMAP-Derived Extent~~L-band Ice Slab Mapping

Figure 11 compares our S-1 derived ~~refrozen ice facie~~ ice slab extent with the ice slab extent derived from SMAP in Miller et al. (2022a). Overall, S-1 offers a significant improvement in both accuracy and resolution, particularly capturing regions in Northwest Greenland that SMAP failed to classify as ice slabs and accurately capturing the elevation bands where ice slabs form in the North and Northeast. However, SMAP does a somewhat better job of capturing the lower limit of the ice slabs in Southwest Greenland, in large part because the lower limit of the SMAP-inferred percolation zone (dark purple ~~dashed~~ outline) is much more consistent with MODIS-inferred estimates of the summer snowline (Ryan et al., 2019) than S-1 (lilac region), which maps wet snow well into the ablation zone in some regions. SMAP also maps melt significantly further inland on the ice sheet than S-1, in part due to the comparatively coarse effective resolution, all of which contributes to different areas in which ice slabs are assumed to be viable.

The upcoming launch of the joint NASA-ISRO NISAR mission scheduled for early 2024 and eventual launch of ESA's Radar Observing System for Europe-L-Band (ROSE-L) mission will ~~soon~~ provide L-band synthetic aperture radar data with high spatial and temporal coverage over Greenland, which has the potential to offer the best of both these products. The enhanced penetration depth at L-band may particularly enable a better delineation of the low-elevation transition from ice slabs to superimposed ice~~and enable more robust constraints on ice slab thickness from space~~. The longer wavelength will also significantly improve interferometric coherence over the ice sheet and potentially enable ice slab mapping based on volume decorrelation (Rizzoli et al., 2017) or other coherence-derived metrics. This will be a particularly important avenue of investiga-

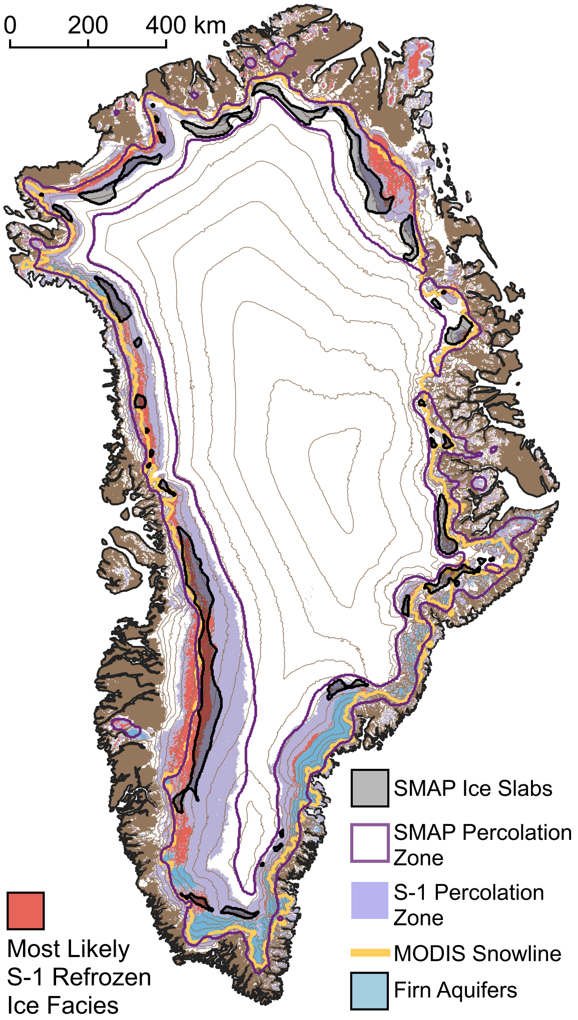

Figure 11. Comparison of S-1 inferred ~~refrozen~~ ice ~~facies~~ slab extent in winter 2016-2017 (this paper) and SMAP-inferred average ice slab extent from 2015-2019 (Miller, 2021). S-1 shows a significant improvement in resolution and accuracy over SMAP. However, SMAP is able to better capture the true extent of the percolation zone, and hence the lower limit of the ice slabs, as demonstrated by the better match between the lower limit of the SMAP-derived percolation zone (Miller, 2021) and a MODIS-derived estimate of the average summer snowline (Ryan et al., 2019). Firn aquifers are shown in light blue (Brangers et al., 2020).

tion given NISAR is expected to primarily collect data in single-polarization mode over Greenland. ~~Additionally~~Unfortunately, NISAR will also not collect data above 77.5° north, ~~unfortunately~~ limiting future capacity to study the rapidly changing northern basins. However, where data are collected, these complementary L-band observations have the potential to significantly improve our capacity to study the near-surface of Greenland from space, and our C-band algorithm development will provide an important bridge between the historical OIB data and future L-band data, which will not overlap in time with OIB. Currently, the limited data catalog of public L-band data collected by ALOS PALSAR over Greenland also offers a valuable opportunity for proof-of-concept studies that can pave the way for NISAR specific algorithms.

5 Conclusions

We have shown that Sentinel-1 winter σ^0_{xpol} and σ^0_{HV} signatures can be used to map the extent of Greenland's ~~refrozen ice facies~~ ice slabs from space at 500 m spatial resolution. Our mapping is in ~~excellent~~ good agreement with both subsurface observations from the OIB ice-penetrating radar data and remote sensing observations of visible surface runoff. We identify new ice slab regions in Southwest Greenland~~and~~, consistent with both firn models and runoff observations, and our mapping suggests that ice slabs are largely ubiquitous in the wet snow zone in all regions besides Southeast Greenland. Given the radiometric stability and consistent calibration efforts for Sentinel-1, we expect that it may be possible to apply the optimized thresholds we derive here for winter 2016-2017 to data collected in other years. However, there is still significant work to be done to assess the interannual radiometric stability of S-1 across the GrIS at various signal-to-noise ratios and to characterize other forms of instrumental uncertainty, particularly due to the evolving observation strategy of S-1 and missing measurements from either S-1A or S-1B in various years. Additionally, evolving conditions on the GrIS, particularly in response to extreme melt (Culberg et al., 2021) and increasing rainfall ~~(Box et al., 2022, 2023)~~(Harper et al., 2023; Box et al., 2023), may significantly alter the subsurface stratigraphy, and therefore the observed backscatter, in ways that are not yet well-understood. Further work in required to fully characterize the physical and dielectric mechanisms that drive C-band sensitivity to firn, ice slabs, and superimposed ice ~~structure~~ structures and how their radiometric signatures may change with time. Future work might also focus on improving the discrimination of crevasses and buried or drained lakes, which can currently lead to misclassifications in ice slab regions. Regardless, the algorithm we develop here lays the groundwork for generating long time series of ice slab expansion from C-band SAR observations with sufficient spatial coverage and resolution to enable long-term monitoring and validation of predictive numerical models.

Data availability. Final Sentinel-1 mosaics (shown in Figure 2) and the final ice slab extent in winter 2016-2017 will be deposited at the NSF Arctic Data Center with a permanent DOI at the time of manuscript acceptance. For the purposes of peer review, the current data sets are temporarily available at: https://drive.google.com/drive/folders/17NzLt60h8iWwQ8JP72mBsYaNFjLhOesx?usp=sharing [Last Access: 2023-11-08]. All Sentinel-1 data were accessed and processed through Google Earth Engine. The data catalog entry can be found at https://developers.google.com/earth-engine/datasets/catalog/COPERNICUS_S1_GRD [Last Access: 2023-11-08]. Ice-penetrating radar detections of slabs are available at https://doi.org/10.5281/zenodo. 7505426 [Last Access: 2023-11-08] (Jullien, 2023). Ice-penetrating radar survey lines and the radargrams shown in Figures 1 and 10 are available from the Center for Remote Sensing and Integrated Systems at https://data.cresis.ku.edu/data/accum/ or through the National Snow and Ice Data Center at https://nsidc.org /data/iracc1b/versions/2 [Last Access: 2023-11-08] (Paden et al., 2014a, b). The elevation of the visible runoff line as a function of time is available at https://zenodo.org /records/6472348 [Last Access: 2023-11-08] (Tedstone, 2022). Sentinel-1 firn aquifer detections are available at https://arcticdata.io/catalog/ view/doi%3A10.18739%2FA2HD7NS8N [Last Access: 2023-11-08] (Brangers et al., 2020). The data used for throughout this paper for basemaps of Greenland are available as follows. The Greenland coastline is available from the British Antarctic Survey at https://data.bas.ac.uk/full-record.php?id=GB/NERC/BAS/PDC/01439 [Last Access: 2023-11-08] (Gerrish, 2020). The ice mask is available through BedMachine Greenland v4 https://sites.ps.uci.edu/morlighem/dataproducts/bedmachine-greenland/ [Last Access: 2023-11-08] (Morlighem et al., 2017). The 200 m elevation contours are derived from ArcticDEM and available at https://www.pgc.umn.edu/data/arcticdem/ [Last Access: 2023-11-08] (Porter et al., 2018).

Author contributions. RC conceived the study, designed and implemented the processing algorithms, and wrote the initial paper draft. RJM and JZM provided guidance and suggestions on the Sentinel-1 processing and ice slab detection workflow. All authors contributed to the scientific analysis of results and writing of the final manuscript.

Competing interests. The contact author has declared that none of the authors has any competing interests.

Acknowledgements. JZM was supported by NASA grants 80NSSC20K1806 and 80NSSC18K1055.

References

Ashcraft, I. and Long, D.: Observation and Characterization of Radar Backscatter over Greenland, IEEE Transactions on Geoscience and Remote Sensing, 43, 225–237, https://doi.org/10.1109/TGRS.2004.841484, 2005.

Ashcraft, I. S. and Long, D. G.: Comparison of Methods for Melt Detection over Greenland Using Active and Passive Microwave Measurements, International Journal of Remote Sensing, 27, 2469–2488, https://doi.org/10.1080/01431160500534465, 2006.

Bader, H.: Sorge's Law of Densification of Snow on High Polar Glaciers, Journal of Glaciology, 2, 319–323, https://doi.org/10.3189/S0022143000025144, 1954.

Barzycka, B., Błaszczyk, M., Grabiec, M., and Jania, J.: Glacier Facies of Vestfonna (Svalbard) Based on SAR Images and GPR Measurements, Remote Sensing of Environment, 221, 373–385, https://doi.org/10.1016/j.rse.2018.11.020, 2019.

Baumgartner, F., Jezek, K. C., Forster, R. R., Gogineni, S. P., and Zabel, I. H. H.: Spectral and Angular Ground-Based Radar Backscatter Measurements of Greenland Snow Facies, in: 1999 IGARSS, 614, pp. 1053–1055, Hamburg, Germany, https://doi.org/10.1109/IGARSS.1999.774530, 1999.

Benson, C. S.: Stratigraphic Studies in the Snow and Firn of the Greenland Ice Sheet, Doctoral Thesis, California Institute of Technology, 1962.

Berger, M., Moreno, J., Johannessen, J. A., Levelt, P. F., and Hanssen, R. F.: ESA's sentinel missions in support of Earth system science, Remote sensing of environment, 120, 84–90, 2012.

Box, J. E., Wehrlé, A., van As, D., Fausto, R. S., Kjeldsen, K. K., Dachauer, A., Ahlstrøm, A. P., and Picard, G.: Greenland Ice Sheet Rainfall, Heat and Albedo Feedback Impacts From the Mid-August 2021 Atmospheric River, Geophysical Research Letters, 49, e2021GL097 356, https://doi.org/10.1029/2021GL097356, 2022.

Box, J. E., Nielsen, K. P., Yang, X., Niwano, M., Wehrlé, A., van As, D., Fettweis, X., Køltzow, M. A. Ø., Palmason, B., Fausto, R. S., van den Broeke, M. R., Huai, B., Ahlstrøm, A. P., Langley, K., Dachauer, A., and Noël, B.: Greenland Ice Sheet Rainfall Climatology, Extremes and Atmospheric River Rapids, Meteorological Applications, 30, e2134, https://doi.org/10.1002/met.2134, 2023.

Brangers, I., Lievens, H., Miège, C., Demuzere, M., Brucker, L., and De Lannoy, G. J.: Sentinel-1 Detects Firn Aquifers in the Greenland Ice Sheet, Geophysical Research Letters, 47, https://doi.org/10.1029/2019GL085192, 2020.

Brils, M., Kuipers Munneke, P., Van De Berg, W. J., and Van Den Broeke, M.: Improved Representation of the Contemporary Greenland Ice Sheet Firn Layer by IMAU-FDM v1.2G, Geoscientific Model Development, 15, 7121–7138, https://doi.org/10.5194/gmd-15-7121-2022, 2022.

Brils, M., Munneke, P. K., Jullien, N., Tedstone, A. J., Machguth, H., van de Berg, W. J., and van den Broeke, M. R.: Climatic Drivers of Ice Slabs and Firn Aquifers in Greenland, Geophysical Research Letters, 51, e2023GL106 613, https://doi.org/10.1029/2023GL106613, 2024.

Culberg, R., Schroeder, D. M., and Chu, W.: Extreme Melt Season Ice Layers Reduce Firn Permeability across Greenland, Nature Communications, 12, 1–9, https://doi.org/10.1038/s41467-021-22656-5, 2021.

Culberg, R., Chu, W., and Schroeder, D. M.: Shallow Fracture Buffers High Elevation Runoff in Northwest Greenland, Geophysical Research Letters, 49, https://doi.org/10.1029/2022GL101151, 2022a.

Culberg, R., Lai, C.-Y., and Michaelides, R.: Ice-Penetrating Radar Observations of Ice Slab Development and Change, 2022b.

Dunmire, D., Banwell, A., Lenaerts, J., and Datta, R. T.: Contrasting Regional Variability of Buried Meltwater Extent over Two Years across the Greenland Ice Sheet, The Cryosphere Discussions, pp. 1–29, https://doi.org/10.5194/tc-2021-3, 2021.

Enderlin, E., Howat, I., Jeong, S., Noh, M.-J., van Angelen, J. H., and van de Broeke, M. R.: An Improved Mass Budget for the Greenland Ice Sheet, Geophysical Research Letters, 41, 866–872, https://doi.org/10.1002/2013GL059010, 2014.

ESA: Sentinel-1 SAR User Guide, Tech. rep., 2023.

Fahnestock, M. A., Bindschadler, R., Kwok, R., and Jezek, K.: Greenland Ice Sheet Surface Properties and Ice Dynamics from ERS-1 SAR Imagery, Science, 262, 1530–1534, 1993.

Fischer, G., Jäger, M., Papathanassiou, K. P., and Hajnsek, I.: Modeling the Vertical Backscattering Distribution in the Percolation Zone of the Greenland Ice Sheet With SAR Tomography, IEEE Journal of Selected Topics in Applied Earth Observations and Remote Sensing, 12, 4389–4405, https://doi.org/10.1109/JSTARS.2019.2951026, 2019.

Forster, R. R., Box, J. E., Van Den Broeke, M. R., Miège, C., Burgess, E. W., Van Angelen, J. H., Lenaerts, J. T., Koenig, L. S., Paden, J., Lewis, C., Gogineni, S. P., Leuschen, C., and McConnell, J. R.: Extensive Liquid Meltwater Storage in Firn within the Greenland Ice Sheet, Nature Geoscience, 7, 95–98, https://doi.org/10.1038/ngeo2043, 2014.

Fox-Kemper, B., Hewitt, H., Xiao, C., Aðalgeirsdóttir, G., Drijfhout, S. S., Edwards, T., Golledge, N., Hemer, M., Kopp, R., Krinner, G., Mix, A., Notz, D., Nowicki, S., Nurhati, I., Ruiz, L., Sallée, J.-B., Slangen, A., and Yu, Y.: Ocean, Cryosphere and Sea Level Change. In Climate Change 2021: The Physical Science Basis, in: Intergovernmental Panel on Climate Change Sixth Assessment Report, chap. Chapter 9, pp. 1211–1362, https://doi.org/10.1017/9781009157896.011.1212, 2021.

Gerrish, L.: The Coastline of Kalaallit Nunaat/ Greenland Available as a Shapefile and Geopackage, Covering the Main Land and Islands, with Glacier Fronts Updated as of 2017, https://doi.org/10.5285/8cecde06-8474-4b58-a9cb-b820fa4c9429, 2020.

Gorelick, N., Hancher, M., Dixon, M., Ilyushchenko, S., Thau, D., and Moore, R.: Google Earth Engine: Planetary-scale Geospatial Analysis for Everyone, Remote Sensing of Environment, 202, 18–27, https://doi.org/10.1016/j.rse.2017.06.031, 2017.

Harper, J., Humphrey, N., Pfeffer, W. T., Brown, J., and Fettweis, X.: Greenland Ice-Sheet Contribution to Sea-Level Rise Buffered by Meltwater Storage in Firn, Nature, 491, 240–243, https://doi.org/10.1038/nature11566, 2012.

Harper, J., Saito, J., and Humphrey, N.: Cold Season Rain Event Has Impact on Greenland's Firn Layer Comparable to Entire Summer Melt Season, Geophysical Research Letters, 50, e2023GL103 654, https://doi.org/10.1029/2023GL103654, 2023.

Herron, M. M. and Langway, C. C.: Firn Densification: An Empirical Model, Journal of Glaciology, 25, 373–385, https://doi.org/10.3189/s0022143000015239, 1980.

Hicks, B. R. and Long, D. G.: Inferring Greenland Melt and Refreeze Severity from SeaWinds Scatterometer Data, International Journal of Remote Sensing, 32, 8053–8080, https://doi.org/10.1080/01431161.2010.532174, 2011.

Hoen, W.: A Correlation-Based Approach to Modeling Interferometric Radar Observations of the Greenland Ice Sheet, Doctoral, Stanford University, 2001.

Hu, J., Zhang, T., Zhou, X., Jiang, L., Yi, G., Wen, B., and Chen, Y.: Extracting Time-Series of Wet-Snow Facies in Greenland Using Sentinel-1 SAR Data on Google Earth Engine, IEEE Journal of Selected Topics in Applied Earth Observations and Remote Sensing, 15, 6190–6196, https://doi.org/10.1109/JSTARS.2022.3192409, 2022.

Humphrey, N. F., Harper, J. T., and Pfeffer, W. T.: Thermal Tracking of Meltwater Retention in Greenland's Accumulation Area, Journal of Geophysical Research: Earth Surface, 117, 1–11, https://doi.org/10.1029/2011JF002083, 2012.

Jezek, K. C., Drinkwater, M. R., Crawford, J. P., Bindschadler, R., and Kwok, R.: Analysis of Synthetic Aperture Radar Data Collected over the Southwestern Greenland Ice Sheet, Journal of Glaciology, 39, 119–132, https://doi.org/10.3189/S002214300001577X, 1993.

Jezek, K. C., Gogineni, P., and Shanableh, M.: Radar Measurements of Melt Zones on the Greenland Ice Sheet, Geophysical Research Letters, 21, 33–36, https://doi.org/10.1029/93GL03377, 1994.

Jullien, N.: Data: Greenland Ice Sheet Ice Slab Expansion and Thickening, https://doi.org/10.5281/zenodo.7505426, 2023.

Jullien, N., Tedstone, A. J., Machguth, H., Karlsson, N. B., and Helm, V.: Greenland Ice Sheet Ice Slab Expansion and Thickening, Geophysical Research Letters, 50, e2022GL100 911, https://doi.org/10.1029/2022GL100911, 2023.

Koenig, L. S., Lampkin, D. J., Montgomery, L. N., Hamilton, S. L., Turrin, J. B., Joseph, C. A., Moutsafa, S. E., Panzer, B., Casey, K. A., Paden, J. D., Leuschen, C., and Gogineni, P.: Wintertime Storage of Water in Buried Supraglacial Lakes across the Greenland Ice Sheet, The Cryosphere, 9, 1333–1342, https://doi.org/10.5194/tc-9-1333-2015, 2015.

Langley, K., Hamran, S. E., Høgda, K. A., Storvold, R., Brandt, O., Hagen, J. O., and Kohler, J.: Use of C-band Ground Penetrating Radar to Determine Backscatter Sources within Glaciers, IEEE Transactions on Geoscience and Remote Sensing, 45, 1236–1245, https://doi.org/10.1109/TGRS.2007.892600, 2007.

Langley, K., Hamran, S.-E., Hogda, K. A., Storvold, R., Brandt, O., Kohler, J., and Hagen, J. O.: From Glacier Facies to SAR Backscatter Zones via GPR, IEEE Transactions on Geoscience and Remote Sensing, 46, 2506–2516, https://doi.org/10.1109/TGRS.2008.918648, 2008.

Langley, K., Lacroix, P., Hamran, S. E., and Brandt, O.: Sources of Backscatter at 5.3 GHz from a Superimposed Ice and Firn Area Revealed by Multi-Frequency GPR and Cores, Journal of Glaciology, 55, 373–383, https://doi.org/10.3189/002214309788608660, 2009.

Li, G., Chen, X., Lin, H., Hooper, A., Chen, Z., and Cheng, X.: Glacier Melt Detection at Different Sites of Greenland Ice Sheet Using Dual-Polarized Sentinel-1 Images, Geo-spatial Information Science, 0, 1–16, https://doi.org/10.1080/10095020.2023.2252034, 2023.

Liang, D., Guo, H., Zhang, L., Cheng, Y., Zhu, Q., and Liu, X.: Time-Series Snowmelt Detection over the Antarctic Using Sentinel-1 SAR Images on Google Earth Engine, Remote Sensing of Environment, 256, 112 318, https://doi.org/10.1016/j.rse.2021.112318, 2021.

Lindsley, R. D. and Long, D. G.: ASCAT and QuikSCAT Azimuth Modulation of Backscatter Over East Antarctica, IEEE Geoscience and Remote Sensing Letters, 13, 1134–1138, https://doi.org/10.1109/LGRS.2016.2572101, 2016.

Long, D. G. and Drinkwater, M. R.: Greenland Ice-Sheet Surface Properties Observed by the Seasat-A Scatterometer at Enhanced Resolution, Journal of Glaciology, 40, 213–230, https://doi.org/10.3189/S0022143000007310, 1994.

Long, D. G. and Miller, J. Z.: Validation of the Effective Resolution of SMAP Enhanced Resolution Backscatter Products, IEEE Journal of Selected Topics in Applied Earth Observations and Remote Sensing, 16, 3390–3404, https://doi.org/10.1109/JSTARS.2023.3260726, 2023.

MacFerrin, M. J., Machguth, H., van As, D., Charalampidis, C., Stevens, C. M., Heilig, A., Vandecrux, B., Langen, P. L., Mottram, R. H., Fettweis, X., van den Broeke, M. R., Pfeffer, W. T., Moussavi, M., and Abdalati, W.: Rapid Expansion of Greenland's Low-Permeability Ice Slabs, Nature, 573, 403–407, https://doi.org/10.1038/s41586-019-1550-3, 2019.

Machguth, H., Macferrin, M., Van As, D., Box, J. E., Charalampidis, C., Colgan, W., Fausto, R. S., Meijer, H. A., Mosley-Thompson, E., and Van De Wal, R. S.: Greenland Meltwater Storage in Firn Limited by Near-Surface Ice Formation, Nature Climate Change, 6, 390–393, https://doi.org/10.1038/nclimate2899, 2016.

Marsh, P. and Woo, M.-K.: Wetting Front Advance and Freezing of Meltwater within a Snow Cover: 1. Observations in the Canadian Arctic, Water Resources Research, 20, 1853–1864, https://doi.org/10.1029/WR020i012p01853, 1984.

Miller, J. Z.: SMAP-derived Perennial Firn Aquifer and Ice Slab Extents 2015-2019, https://doi.org/10.5281/zenodo.8380493, 2021.

Miller, J. Z., Culberg, R., Long, D. G., Shuman, C. A., Schroeder, D. M., and Brodzik, M. J.: An Empirical Algorithm to Map Perennial Firn Aquifers and Ice Slabs within the Greenland Ice Sheet Using Satellite L-band Microwave Radiometry, The Cryosphere, 16, 103–125, https://doi.org/10.5194/tc-16-103-2022, 2022a.

Miller, J. Z., Long, D. G., Shuman, C. A., Culberg, R., Hardman, M. A., and Brodzik, M. J.: Mapping Firn Saturation Over Greenland Using NASA's Soil Moisture Active Passive Satellite, IEEE Journal of Selected Topics in Applied Earth Observations and Remote Sensing, 15, 3714–3729, https://doi.org/10.1109/JSTARS.2022.3154968, 2022b.

Morlighem, M., Williams, C. N., Rignot, E., An, L., Arndt, J. E., Bamber, J. L., Catania, G., Chauche, N., Dowdeswell, J. A., Dorschel, B., Fenty, I., Hogan, K., Howat, I., Hubbard, A., Jakobsson, M., Jordan, T. M., Kjeldsen, K. K., Millian, R., Mayer, L., Mouginto, J., Noel, B. P. Y., O'Cofaigh, C., Palmer, S., Rysgaard, S., Seroussi, H., Siegert, M. J., Slabon, P., Straneo, F., van den Broeke, M. R., Weinrebe, W., Wood, M., Zinglersen, K. B., Chauché, N., Dowdeswell, J. A., Dorschel, B., Fenty, I., Hogan, K., Howat, I., Hubbard, A., Jakobsson, M., Jordan, T. M., Kjeldsen, K. K., Millan, R., Mayer, L., Mouginot, J., Noël, B. P., O'Cofaigh, C., Palmer, S., Rysgaard, S., Seroussi, H., Siegert, M. J., Slabon, P., Straneo, F., van den Broeke, M. R., Weinrebe, W., Wood, M., and Zinglersen, K. B.: BedMachine v3: Complete Bed Topography and Ocean Bathymetry Mapping of Greenland From Multibeam Echo Sounding Combined With Mass Conservation, Geophysical Research Letters, 44, 11,051–11,061, https://doi.org/10.1002/2017GL074954, 2017.

Mouginot, J., Rignot, E., Bjørk, A. A., van den Broeke, M., Millan, R., Morlighem, M., Noël, B., Scheuchl, B., and Wood, M.: Forty-Six Years of Greenland Ice Sheet Mass Balance from 1972 to 2018, Proceedings of the National Academy of Sciences of the United States of America, 116, 9239–9244, https://doi.org/10.1073/pnas.1904242116, 2019.

Munneke, P. K., M. Ligtenberg, S. R., van den Broeke, M. R., van Angelen, J. H., and Forster, R. R.: Explaining the Presence of Perennial Liquid Water Bodies in the Firn of the Greenland Ice Sheet, Geophysical Research Letters, 41, 476–483, https://doi.org/10.1002/2013GL058389, 2014.

Nagler, T. and Rott, H.: Retrieval of Wet Snow by Means of Multitemporal SAR Data, IEEE Transactions on Geoscience and Remote Sensing, 38, 754–765, https://doi.org/10.1109/36.842004, 2000.

Noël, B., van de Berg, W. J., Lhermitte, S., and van den Broeke, M. R.: Rapid Ablation Zone Expansion Amplifies North Greenland Mass Loss, Science Advances, 5, 2–11, https://doi.org/10.1126/sciadv.aaw0123, 2019.

Paden, J., Li, J., Rodriguez-Morales, F., and Hale, R.: IceBridge MCoRDS Radar L1B Geolocated Radar Echo Strength Profiles, Version 2 [2015_Greenland_C130], https://doi.org/10.5067/90S1XZRBAX5N, 2014a.

Paden, J., Li, J., Rodriguez-Morales, F., and Hale, R.: IceBridge Accumulation Radar L1B Geolocated Radar Echo Strength Profiles, Version 2 [2017_Greenland_P3], https://doi.org/10.5067/0ZY1XYHNIQNY, 2014b.

Partington, K. C.: Discrimination of Glacier Facies Using Multi-Temporal SAR Data, Journal of Glaciology, 44, 42–53, https://doi.org/10.3189/S0022143000002331, 1998.

Pfeffer, W. T. and Humphrey, N. F.: Formation of Ice Layers by Infiltration and Refreezing of Meltwater, Annals of Glaciology, 26, 83–91, https://doi.org/10.3189/1998aog26-1-83-91, 1998.

Porter, C., Morin, P., Howat, I., Noh, M.-J., Bates, B., Peterman, K., Keesey, S., Schlenk, M., Gardiner, J., Tomko, K., Willis, M., Kelleher, C., Cloutier, M., Husby, E., Foga, S., Nakamura, H., Platson, M., Wethington, M., Williamson, C., Bauer, G., Enos, J., Arnold, G., Kramer, W., Becker, P., Doshi, A., D'Souza, C., Cummens, P., Laurier, F., and Bojesen, M.: ArcticDEM, V1, https://doi.org/10.7910/DVN/OHHUKH, 2018.

Rignot, E.: Backscatter Model for the Unusual Radar Properties of the Greenland Ice Sheet, Journal of Geophysical Research: Planets, 100, 9389–9400, https://doi.org/10.1029/95JE00485, 1995.

Rignot, E., Echelmeyer, K., and Krabill, W.: Penetration Depth of Interferometric Synthetic-Aperture Radar Signals in Snow and Ice, Geophysical Research Letters, 28, 3501–3504, https://doi.org/10.1029/2000GL012484, 2001.

Rignot, E. J., Ostro, S. J., van Zyl, J. J., and Jezek, K. C.: Unusual Radar Echoes from the Greenland Ice Sheet, Science, 261, 1710–1713, https://doi.org/10.1126/science.261.5129.1710, 1993.

Rizzoli, P., Martone, M., Rott, H., and Moreira, A.: Characterization of Snow Facies on the Greenland Ice Sheet Observed by TanDEM-X Interferometric SAR Data, Remote Sensing, 9, 315, https://doi.org/10.3390/rs9040315, 2017.

Ryan, J. C., Smith, L. C., Van As, D., Cooley, S. W., Cooper, M. G., Pitcher, L. H., and Hubbard, A.: Greenland Ice Sheet Surface Melt Amplified by Snowline Migration and Bare Ice Exposure, Science Advances, 5, 1–11, https://doi.org/10.1126/sciadv.aav3738, 2019.

Swift, C. T., Hayes, P. S., Herd, J. S., Jones, W. L., and Delnore, V. E.: Airborne Microwave Measurements of the Southern Greenland Ice Sheet, Journal of Geophysical Research: Solid Earth, 90, 1983–1994, https://doi.org/10.1029/JB090iB02p01983, 1985.

Tedesco, M. and Fettweis, X.: Unprecedented Atmospheric Conditions (1948–2019) Drive the 2019 Exceptional Melting Season over the Greenland Ice Sheet, The Cryosphere, 14, 1–26, https://doi.org/10.5194/tc-2019-254, 2020.

Tedstone, A.: Increasing Surface Runoff from Greenland's Firn Areas, https://doi.org/10.5281/zenodo.6472348, 2022.

Tedstone, A. J. and Machguth, H.: Increasing Surface Runoff from Greenland's Firn Areas, Nature Climate Change, 12, 672–676, https://doi.org/10.1038/s41558-022-01371-z, 2022.

Ulaby, F. T. and Long, D. G.: Microwave Radar and Radiometric Remote Sensing, The University of Michigan Press, Ann Arbor, MI, 2014.

Van Den Broeke, M., Bamber, J., Ettema, J., Rignot, E., Schrama, E., Van Berg, W. J. D., Van Meijgaard, E., Velicogna, I., and Wouters, B.: Partitioning Recent Greenland Mass Loss, Science, 326, 984–986, https://doi.org/10.1126/science.1178176, 2009.

Vollrath, A., Mullissa, A., and Reiche, J.: Angular-Based Radiometric Slope Correction for Sentinel-1 on Google Earth Engine, Remote Sensing, 12, 1867, https://doi.org/10.3390/rs12111867, 2020.

Wismann, V.: Monitoring of Seasonal Snowmelt on Greenland with ERS Scatterometer Data, IEEE Transactions on Geoscience and Remote Sensing, 38, 1821–1826, https://doi.org/10.1109/36.851766, 2000.